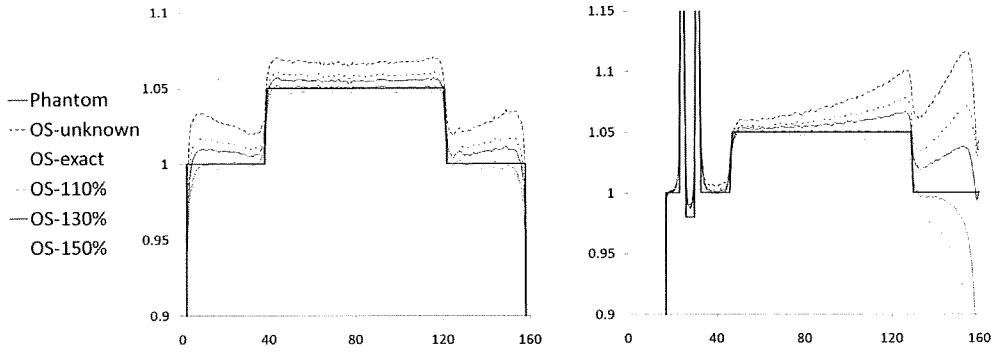

Fig. 4 Central horizontal (left) and vertical (right) profiles of ROI images shown in Fig. 3.

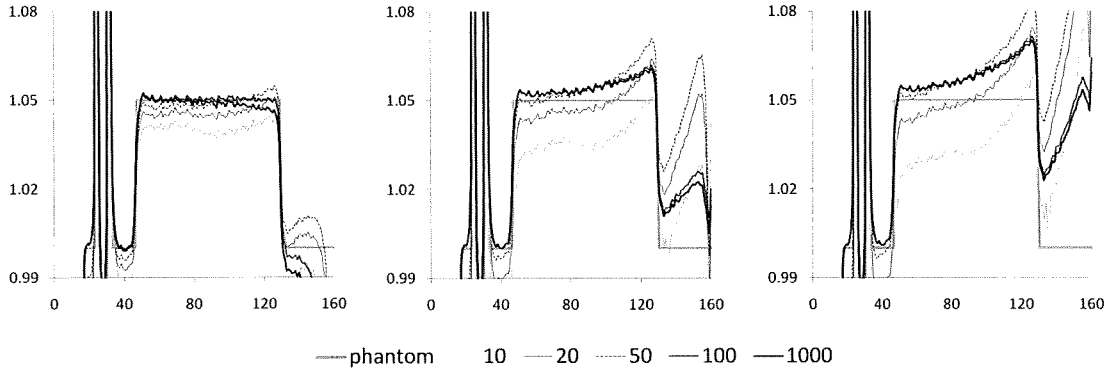

Fig. 5 Central vertical profiles of the reconstructed ROI images with different degrees of OS accuracy corresponding to 110% (left), 130% (middle) and 150% (right) using 10, 20, 50, 100, and 1000 iterations of OSEM algorithm with 8 subsets.

observed if we iterate more, from which we found that 10 or 20 iterations are not enough in the current problem. We also found that the necessary iteration number to achieve sufficient image quality did not depend very much on the OS accuracy as long as the OS is changed from "exact" to "150% OS". Furthermore, the convergence speed of the proposed algorithm with automatic OS estimation (detailed below in section 3.2) was only a bit slower compared to the cases where the OS is *a priori* known. From this experimental study (to determine the necessary iteration number) and the fact that the iterative algorithm with more than 100 iterations is not practical anymore, we performed all the simulation studies with 100 iterations.

2) Proposed iterative algorithm study

The ordered subsets version of the proposed algorithm, detailed above in section 2.3, was evaluated in comparison to the conventional OSEM algorithm. In this study, the FORBILD thorax phantom was modified by adding low-contrast hot/cold spots in the cardiac region to evaluate the effect of low-frequency artifacts. Other simulation parameters were similar to that in the previous study. The following three different scenarios were investigated. The first one assumes that the OS is exactly known (the ideal case) and reconstruction is done using the conventional OSEM algorithm. In the second and third scenarios, reconstruction is done using the OSEM and Th-OSEM with no *a priori* knowledge of the OS, respectively. Reconstructed ROIs for the noise free data and the data with added Poisson noise are shown in **Fig. 6** and the corresponding profiles are plotted in **Fig. 7**. The same image trimming as that in **Fig. 3** was used for display. It is clear that the proposed algorithm successfully reduces the DC-shift and low-frequency artifacts when the OS is unknown thanks to the automatic estimation of the OS.

From the reconstructed images in **Fig. 6** and the corresponding profiles in **Fig. 7**, it is noticed that the upper part of the ROI (close to the object boundary) suffers from less DC/low-frequency artifacts than the lower part (located at the center of object). In the followings we explain this phenomenon. It is known that the stability of inversion for

this reconstruction problem depends on the position of pixel inside the ROI. The inversion is more stable for the pixels located close to the upper part of the ROI (close to the object boundary), but the stability of inversion becomes unstable for the pixels located at the lower part (located at the center of object). This fact has been theoretically clarified by using the analytical continuation technique in [8] (please see **Fig. 5** of reference [8]). Here, we give an intuitive explanation for this variation in the stability from the view point of iterative reconstruction. For the pixels located at the upper part of the ROI, the boundary of OS is close so that the *a priori* knowledge that "the object is zero outside the OS" is quickly propagated to the pixels during iterative reconstruction, which result in better stability of inversion. However, for the pixels located at the lower part of the ROI, the closest OS is distant so that further iterations are necessary for the *a priori* knowledge to propagate to the reconstructed pixels, which result in worse stability.

From practical point-of-view, it is possible to correctly estimate a portion of the OS (corresponding to the top side of the object in the previous simulation study) from the truncated projection data directly by detecting the zero projection rays. However, by such simple method, the bottom side of the OS cannot be estimated from the truncated projection data. We verified that the top side of the OS alone is insufficient to get reconstruction comparable to **Fig. 6**(c). Moreover, such a simple method is not valid if the object is non-convex or the ROI is located completely inside the object (interior problem). A clinical example of this setup was studied here by modifying the phantom to simulate a female patient. In this setup, all the projection views suffer from the truncation in both the right and left portions. Even in this difficult setup, the solution is still unique if the OS is accurately known [8] . We simulated the same imaging setups as those of the previous studies and the results are presented in **Fig. 8**. Even with this challenging setup, the Th-OSEM behaves well and could reduce the artifacts in the reconstructed ROI.

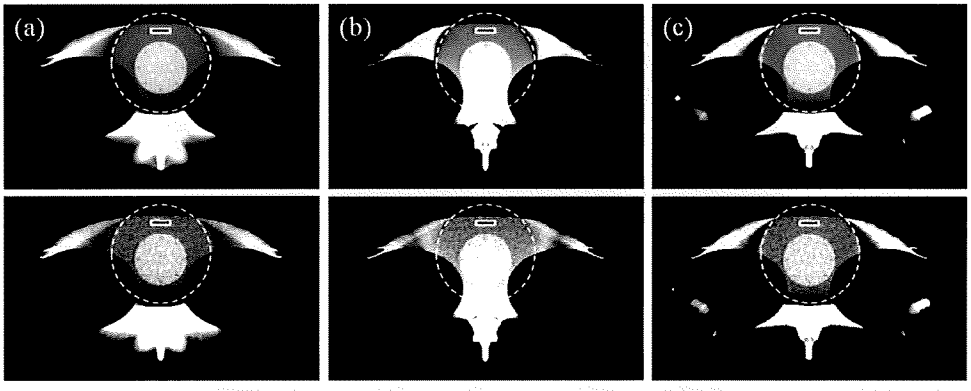

Fig. 6 Reconstructed ROIs by using (a) OSEM with the exact OS, (b) OSEM with the unknown OS and (c) Th-OSEM with the unknown OS. The top row shows reconstructions with noise free data and the bottom row shows reconstruction with added Poisson noise. The display gray scale is [0.95, 1.07].

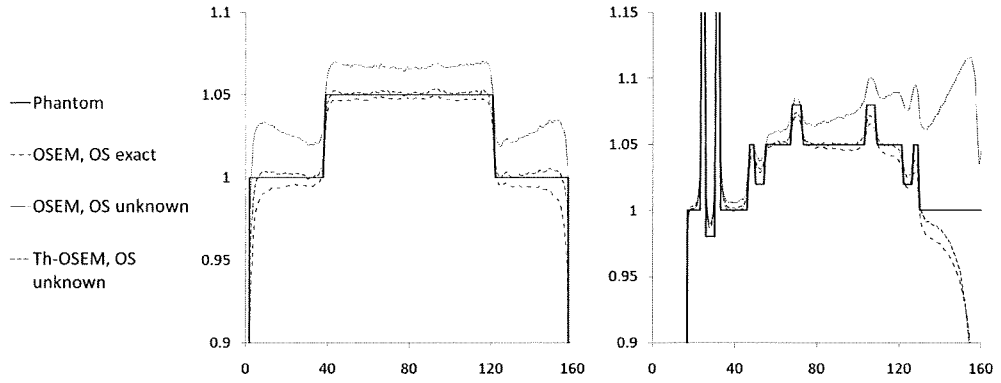

Fig. 7 Central horizontal (left) and vertical (right) profiles for ROI images shown in **Fig. 5** (top row).

In the simulation study to investigate the effect of OS accuracy on image quality (section 3.1), we assumed that the OS is known (with various degrees of accuracy) and used only the *a priori* knowledge that "the value of object is zero outside the known OS" (no *a priori* knowledge corresponding to the value of object inside the OS was used). On the other hand, in the simulation study to investigate the ability of the proposed algorithm (section 3.2), we assumed that the OS is unknown, because the purpose of this algorithm is to automatically estimate the OS. In other words, the proposed algorithm requires no *a priori* knowledge (except for the fact that the object has a finite support, which can be satisfied in every situation of CT imaging).

3) Real data

This study was done using a real data obtained from Siemens sensation 64 slice CT scanner using a 30×20×10 cm anthropomorphic chest phantom (QRM-thorax, QRM GmBH, Mohrendorf, Germany) shown in **Fig. 9**(d). The phantom consists of artificial lung lobes, shell of soft tissue equivalent material, tissue equivalent cardiac insert, and a spine insert, to which two water bottles were attached to represent the arms. Projection data was measured using the fan-beam geometry with 1,160 views (over 360°) and 672 detector channels. The projection data was rebinned into parallel-beam with 580 views (over 180°) and 672 radial bins. Image grid corresponding to the whole image was set to of 672×672 pixels and the ROI was selected as a circular region with a radius of 200 pixels covering the cardiac insert region. First, the FBP algorithm was used to reconstruct the whole object using the full scan data as shown in **Fig. 9**(a). Then a reconstruction was performed for ROI imaging using the OSEM and Th-OSEM

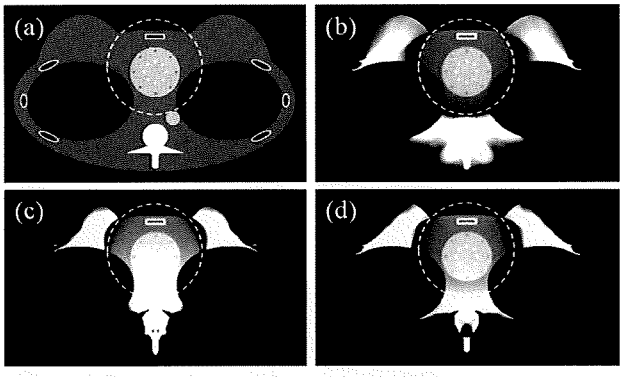

Fig. 8 (a) The modified phantom. Reconstructed ROIs using (b) OSEM with the exact OS, (c) OSEM with the unknown OS, and (d) Th-OSEM with the unknown OS. The display gray scale is [0.95 1.07].

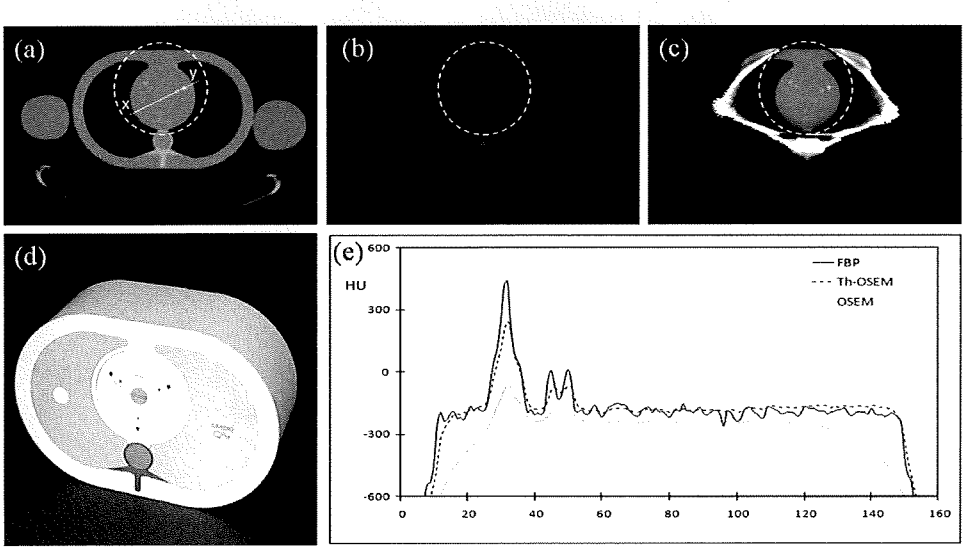

Fig. 9 Reconstructed images by using (a) FBP algorithm with the full scan, (b) OSEM with the ROI scan and (c) Th-OSEM with the ROI scan. The display window is set to [-480HU, 560HU]. (d) The original QRM-Thorax physical phantom (image from www.qrm.de). (e) Profiles corresponding to the white line segment (x-y) shown in (a).

algorithms with 16 subsets and 50 iterations without including the OS constraint. Reconstructed ROI images using OSEM and Th-OSEM are shown in **Fig. 9**(b) and (c), respectively. In **Fig. 9**, the reconstructed whole image matrix was trimmed to the ROI image consisting of 672×430 pixels for display. The results indicate a significant improvement in reducing the DC-shift and low-frequency artifacts when the Th-OSEM is employed.

4. Conclusions

The target of this work was to investigate the effect of OS constraint to the quality of reconstructed images from truncated projection data. This study implies that the lack of OS knowledge introduces DC-shift and low-frequency artifacts in the reconstructed images when the projection data is truncated. These artifacts decrease relative to the degree of OS accuracy. Moreover, we proposed an iterative algorithm that includes a sparsity constraint during the iteration in the form of thresholding function. This algorithm succeeded in reducing the artifacts thanks to its ability to automatically estimate the OS during reconstruction. The simulation results for noise free and noisy data show that the use of the proposed algorithm satisfactorily reduces the DC-shift and low-frequency artifacts even for the case where the OS is completely unknown. Moreover, the similar image improvements were achieved under more difficult configurations such as the non-convex object. The similar image improvements were also obtained by using the real data corresponding to the physical thorax phantom. The proposed algorithm is relatively simple and easy to be implemented and its extension to 3D reconstruction is also possible.

References

〔1〕 Brenner DJ, Hall EJ: Computed Tomography – An increasing source of radiation exposure. N Engl J Med **357**: 2277-2284, 2007

〔2〕 Lewitt RM: Processing of incomplete measurement data in computed tomography. Med Phys **6**: 412-417, 1979

〔3〕 Ogawa K, Nakajima M, Yuta S: A reconstruction Algorithm from Truncated Projections. IEEE Trans Med Imag **3**: 34-40, 1984

〔4〕 Ohnesorge B, Flohr T, Schwarz K et al: Efficient correction for CT image artifacts caused by objects extending outside the scan field of view. Med Phys **27**: 39-46, 2000

〔5〕 Zhang B, Zeng GL: Two-dimensional iterative region-of-interest (ROI) reconstruction from truncated projection data. Med Phys **34**: 935-944, 2007

〔6〕 Noo F, Clackdoyle R, Pack JD: A two-step Hilbert transform method for 2D image reconstruction. Phys Med Biol **49**: 3903-3923, 2004

〔7〕 Pan X, Zou Y, Xia D: Image reconstruction in peripheral and central regions-of-interest and data redundancy. Med Phys **32**: 673-684, 2005

〔8〕 Defrise M, Noo F, Clackdoyle R et al: Truncated Hilbert transform and image reconstruction from limited tomographic data. Inverse Problems **22**: 1037-1053, 2006

〔9〕 Kudo H, Courdurier M, Noo F et al: Tiny *a priori* knowledge solves the interior problem in computed tomography. Phys Med Biol **53**: 2207-2231, 2008

〔10〕 Ye Y, Yu H, Wei Y et al: A general local reconstruction approach based on a truncated Hilbert transform. Int J Biomed Imaging **2007**: Article ID 63634, 8 pages, 2007

〔11〕 Gregoriou GK, Tsui BMW, Gullberg GT: Effect of truncated projections on defect detection in attenuation-compensated fanbeam cardiac SPECT. J Nucl Med **39**: 166-175, 1998

〔12〕 Zeniya T, Watabe H, Sohlberg A et al: 3D-OSEM reconstruction from truncated data in pinhole SPECT. Conference Record of 2007 IEEE Medical Imaging Conference: Paper No. M25-1, 2007

〔13〕 Natterer F: The Mathematics of Computerized Tomography. SIAM, Philadelphia, 2001

〔14〕 Donoho DL: Compressed sensing. IEEE Trans Inf Theory **52**: 1289-1306, 2006

〔15〕 Mameuda Y, Kudo H: New anatomical-prior-based image reconstruction method for PET/SPECT. Conference Record of 2007 IEEE Medical Imaging Conference: Paper No. M23-2, 2007

〔16〕 Leng S, Tang J, Zambelli J et al: High temporal resolution and streak-free four-dimensional cone-beam computed tomography. Phys Med Biol **53**: 5653-5673, 2008

〔17〕 Trzasko J, Manduca A: Highly undersampled magnetic resonance image reconstruction via homotopic ℓ_0-minimization. IEEE Trans Med Imag **28**: 106-121, 2009

〔18〕 Li M, Yang H, Kudo H: An accurate iterative reconstruction algorithm for sparse objects: application to 3D blood-vessel reconstruction from a limited number of projections. Phys Med Biol **47**: 2599-2609, 2002

〔19〕 Daubechies I, Defrise M, De Mol C: An iterative thresholding algorithm for linear inverse problems with a sparsity constraint. Comm Pure Appl Math **57**: 1413-1457, 2004

〔20〕 Browne J, De Pierro AR: A row-action alternative to the EM algorithm for maximizing likelihoods in emission tomography. IEEE Trans Med Imag **15**: 687-699, 1996

〔21〕 Bertsekas DP: Nonlinear Programming. Athena Scientific, 1995

物体境界未知下におけるトランケーションCT投影データからの逐次近似法による関心領域画像再構成

イサム A. ラシド[*1] 工藤博幸[*1] フレデリック ヌー[*2]

[*1] 筑波大学大学院システム情報工学研究科コンピュータサイエンス専攻
[*2] ユタ大学放射線科

要旨：本論文では，トランケーションされたCT投影データからの画像再構成を取り扱う．X線を関心領域（ROI）のみに照射してROI画像を撮影するROIイメージングでは，投影データがトランケーションされ画像再構成は解が一意に定まりにくい難しい問題となる．最近開発された微分逆投影（DBP）の理論によりROIのサイズと配置によってはトランケーションされた投影データから厳密な画像再構成が可能な場合があることが示されたが，物体境界が事前に既知であることが前提となっている．しかし，実際のイメージング状況では物体境界が正確にわからない場合が多い．本論文では，(1) トランケーションされた投影データからの画像再構成において事前情報として用いる物体境界の精度と再構成画像のアーティファクトの関係を評価すること，(2) 逐次近似画像再構成の反復計算の過程において物体境界を自動推定しアーティファクトを低減する新しい画像再構成法を提案すること，の2つを目的とする．新しい手法では，画像再構成のコスト関数に画像のL0ノルムを加えることで物体境界の推定を実現している．シミュレーション実験と実データによる実験を行い，提案手法を用いることによりアーティファクトが大幅に低減できることを示す．

キーワード：トモグラフィ，画像再構成，ROIイメージング，トランケーション投影データ，物体境界
Med Imag Tech **27**(5): 321-331, 2009

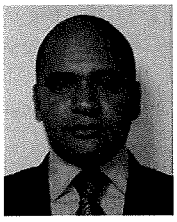

Essam A. Rashed（イサム ラシド）
Received his B.Sc. in scientific computing (with honors) and M.Sc. in computer science in 1998 and 2002 from Suez Canal Univ., Egypt, respectively. Now, he is with the doctoral program in systems and information engineering, Univ. of Tsukuba. His research interests include computed tomography and medical image processing. He is a winner of the Egyptian Government national scholarship (2006) and JAMIT best presentation award (2008). He is a member of IEEE NPSS and JAMIT.

Frédéric Noo（フレデリック ヌー）
Frédéric Noo, PhD., is a Tenured Associate Professor of Radiology at the University of Utah, where he joined the Utah Center for Advanced Imaging Research (UCAIR) in 2001. His specialty is x-ray computed tomography on which he described 126 original contributions in various journals and at conferences.

工藤博幸（くどう ひろゆき）
1985年東北大・工・通信卒．1990年同大大学院博士課程了．現在，筑波大・システム情報・教授．1990年電子情報通信学会論文賞，1991年・2001年・2006年・2008年日本医用画像工学会論文賞，2006年・2008年国際雑誌『Inverse Problems』High Lights，2008年国際雑誌『Physics in Medicine and Biology』High Lights受賞．工博．CTとPETを中心とした医用イメージング，画像処理の研究に従事．IEEE，電子情報通信学会，各会員．2008年にCTの未解決問題であるInterior Problemの安定な厳密解法を発見し，これに関する2つの論文が国際雑誌『Physics in Medicine and Biology』と『Inverse Problems』の2008 High Lightsを受賞した．

* * *

articles

molecular pharmaceutics

Nitroxyl Radicals for Labeling of Conventional Therapeutics and Noninvasive Magnetic Resonance Imaging of Their Permeability for Blood–Brain Barrier: Relationship between Structure, Blood Clearance, and MRI Signal Dynamic in the Brain

Zhivko Zhelev,[†] Rumiana Bakalova,*[,†] Ichio Aoki,[†] Ken-ichiro Matsumoto,[‡] Veselina Gadjeva,[§] Kazunori Anzai,[‡] and Iwao Kanno[†]

Department of Biophysics, Molecular Imaging Center, and Center for Heavy-ion Particle Therapy, National Institute of Radiological Sciences, 4-9-1 Anagawa, Inage-ku, Chiba 263-8555, Japan, and Department of Chemistry and Biochemistry, Trakia University, Stara Zagora, Bulgaria

Received September 24, 2008; Revised Manuscript Received January 7, 2009; Accepted January 9, 2009

Abstract: The present study describes a novel nonradioactive methodology for *in vivo* noninvasive, real-time imaging of blood–brain barrier (BBB) permeability for conventional drugs, using nitroxyl radicals as spin-labels and magnetic resonance imaging (MRI). Two TEMPO-labeled analogues (SLENU and SLCNUgly) of the anticancer drug lomustine [1-(2-chloroethyl)-3-cyclohexyl-1-nitrosourea] were synthesized, using a substitution of the cyclohexyl part with nitroxyl radical. Nonmodified nitroxyl radical TEMPOL was used for comparison. The nitroxyl derivatives were injected intravenously in healthy mice via the tail vein, and MR imaging of the brain was performed on a 7.0 T MRI. The MRI signal dynamic of SLENU and SLCNUgly followed the same kinetics as nonmodified TEMPO radical. SLENU and SLCNUgly were rapidly transported and randomly distributed in the brain tissue, which indicated that the exchange of cyclohexyl part of lomustine with TEMPO radical did not suppress the permeability of the anticancer drug for BBB. The selected nitroxyl derivatives possessed different hydrophobicity, cell permeabilization ability, and blood clearance. Based on these differences, we investigated the relationship between the structure of nitroxyl derivatives, their half-life in the circulation, and their MRI signal dynamic in the brain. This information was important for estimation of the merits and demerits of the described methodology and finding pathways for overcoming the restrictions.

Keywords: Nitroxyl radicals; lomustine; magnetic resonance imaging; electron-paramagnetic resonance imaging; blood–brain barrier permeability

Introduction

The nitroxyl radicals are well-known from electron-paramagnetic resonance (EPR) studies.[1−6] In 1984, it was reported that nitroxyl radicals possess comparatively high T_1 contrast properties and could be also applied in magnetic resonance imaging (MRI).[2,7] The nitroxyls are small molecules, sensitive to the reduction status of biological samples, and their use in life science research is limited predominantly to tissue oxygen and redox mapping *in vitro* and *in vivo*.[3−6,8−13] The paramagnetic nitroxyl radical could be reduced to diamagnetic hydroxylamine with a loss of EPR signal or ^{1}H-MRI relaxation time and thus serve as a reduction sensor. However, the diamagnetic hydroxylamine

* Author to whom correspondence should be addressed. Rumiana Bakalova, PhD, Department of Biophysics, Molecular Imaging Center, National Institute of Radiological Sciences (NIRS), 4-9-1 Anagawa, Inage-ku, Chiba 263-8555, Japan. Tel: +81-43-206-4067. Fax: +81-43-206-3276. E-mail: bakalova@nirs.go.jp; ra_bakalova@yahoo.com.

† Department of Biophysics, Molecular Imaging Center, National Institute of Radiological Sciences.

‡ Center for Heavy-ion Particle Therapy, National Institute of Radiological Sciences.

§ Trakia University.

(1) Griffeth, L. K.; Rosen, G. M.; Rauckman, E. J.; Drayer, B. P. Pharmacokinetics of nitroxide NMR contrast agents. *Invest. Radiol.* **1984**, *19*, 553–562.

10.1021/mp800175k CCC: $40.75 © 2009 American Chemical Society
Published on Web 02/10/2009

Scheme 1. Nitroxyl Radical Reduction and Oxidation Sensors

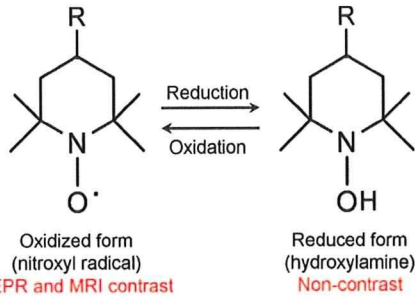

could be reconverted via oxygenation to paramagnetic nitroxyl radical with an appearance of EPR or ^{1}H-MRI relaxivity and thus serve as an oxidation sensor. The rate constants of both processes could be used for evaluation of reduction/oxidation balance in cells and tissues, using EPR imaging (EPRI) or MRI (Scheme 1).

Some nitroxyl radicals can easily gain an excellent cell permeability and even a permeability for blood−brain barrier (BBB) by simple chemical modification.[11−15] All these characteristics make them attractive for MRI diagnostics, and their application in life science research could be extended beyond the limits, mentioned above. In this context, we supposed that the nitroxyl radicals could be appropriate spin-labels of conventional therapeutics: for noninvasive MR imaging of their permeability for BBB and their localization in different organs and tissues. Most EPR studies, targeting the brain, have employed pyrrolidine-type (PROXYL-type) nitroxyl radicals, which have a higher stability *in vivo* in comparison with piperidine-type (TEMPO-type) nitroxyl radicals due to the low temporal resolution of CW-based techniques.[12−15] The higher temporal resolution of MRI allows an observation of pharmacokinetics of piperidine-type nitroxyl radicals.[9,16] In addition, MRI is characterized by much higher spatial resolution than EPRI and gives an excellent anatomical reference, which could facilitate the exact localization of a nitroxyl-labeled drug in the organism. Below, we would like to describe the impact of this approach and to give a proof for the reality of this concept.

The noninvasive, real-time imaging of drug permeability for BBB and localization in different brain compartments (drug brain mapping) is an indispensible step in the preclinical and clinical testing of new therapeutics for brain diseases. The precise mapping of a drug in the target or nontarget tissue has a significant impact for its dosing and prognostication of its target-specific effect and side effects.

The conventional methods for investigation of BBB permeability are usually invasive and time- and cost-consuming, often suffering from artifacts, and requiring a large number of experimental animals.[17−22] *In vitro* models of BBB (e.g., cell and tissue cultures, immobilized artificial

(2) Keana, J. F.; Pou, S.; Rosen, G. M. Nitroxides as potential contrast enhancing agents for MRI application: influence of structure on the rate of reduction by rat hepatocytes, whole liver homogenate, subcellular fractions, and ascorbate. *Magn. Reson. Med.* **1987**, *5*, 525–536.

(3) Valgimigli, L.; Pedulli, G. F.; Paolini, M. Measurement of oxidative stress by EPR radical-probe technique. *Free Radical Biol. Med.* **2001**, *31*, 708–716.

(4) Utsumi, H.; Yamada, K. In vivo electron spin resonance-computed tomography/nitroxyl probe technique for non-invasive analysis of oxidative injuries. *Arch. Biochem. Biophys.* **2003**, *416*, 1–8.

(5) Takeshita, K.; Ozawa, T. Recent progress in in vivo ESR spectroscopy. *J. Radiat. Res. (Tokyo)* **2004**, *45*, 373–384.

(6) Soule, B. P.; Hyodo, F.; Matsumoto, K.; Simone, N. L.; Cook, J. A.; Krishna, M. C.; Mitchell, J. B. Therapeutic and clinical applications of nitroxide compounds. *Antioxid. Redox Signaling* **2007**, *9*, 1731–1743.

(7) Afzal, V.; Brasch, R. C.; Nitecki, D. E.; Wolff, S. Nitroxyl spin label contrast enhancers for magnetic resonance imaging. Studies of acute toxicity and mutagenesis. *Invest. Radiol.* **1984**, *19*, 549–552.

(8) Matsumoto, K.; Hyodo, F.; Matsumoto, A.; Koretsky, A. P.; Sowers, A. L.; Mitchell, J. B.; Krishna, M. C. High-resolution mapping of tumor redox status by MRI using nitroxides as redox-sensitive contrast agents. *Clin. Cancer Res.* **2006**, *12*, 2455–2462.

(9) Hyodo, F.; Matsumoto, K.; Matsumoto, A.; Mitchel, J. B.; Krishna, M. C. Probing the intracellular redox status of tumors with MRI and redox-sensitive contrast agents. *Cancer Res.* **2006**, *66*, 9921–9928.

(10) Hyodo, F.; Matsumoto, K.; Matsumoto, A.; Mitchel, J. B.; Krishna, M. C. Probing the intracellular redox status of tumors with MRI and redox-sensitive contrast agents. *Cancer Res.* **2006**, *66*, 9921–9928.

(11) Hyodo, F.; Chuang, K.-H.; Goloshevsky, A. G.; Sulima, A.; Griffiths, G. L.; Mitchell, J. B.; Koretsky, A. P.; Krishna, M. C. Brain redox imaging using blood-brain barrier-permeable nitroxide MRI contrast agent. *J. Cereb. Blood Flow Metab.* **2008**, 1–10.

(12) Myiake, M.; Shen, J.; Liu, S.; Shi, H.; Liu, W.; Yuan, Z.; Pritchard, A.; Kao, J. P. Y.; Liu, K. J.; Rosen, G. M. Acetoxymethoxycarbonyl nitroxides as EPR proimaging agents to measure O2 levels in mouse brain: A pharmacokinetic and pharmacodynamic study. *J. Pharmacol. Exp. Ther.* **2006**, *318*, 1187–1193.

(13) Shen, J.; Liu, S.; Miyake, M.; Liu, W.; Pritchard, A.; Kao, J. P. Y.; Rosen, G. M.; Tong, Y.; Liu, K. J. Use of 3-acetoxymethoxycarbonyl-2,2,5,5-tetramethyl-1-pyrrolidinyloxyl as an EPR oximetry probe: Potential for in vivo measurement of tissue oxygenation in mouse brain. *Magn. Reson. Med.* **2006**, *55*, 1433–1440.

(14) Sano, H.; Naruse, M.; Matsumoto, K.; Oi, T.; Utsumi, H. A new nitroyxl-probe with high retention in the brain and its application for brain imaging. *Free Radical Biol. Med.* **2000**, *28*, 959–969.

(15) Anzai, K.; Saito, K.; Takeshita, K.; Takahashi, S.; Miyazaki, H.; Shoji, H.; Lee, M. C.; Masumizu, T.; Ozawa, T. Assessment of ESR-CT imaging by comparison with autoradiography for the distribution of a blood-brain-barrier permeable spin probe, MC-PROXYL, to rodent brain. *Magn. Reson. Imaging* **2003**, *21*, 765–772.

(16) Cotrim, A. P.; Hyodo, F.; Matsumoto, K.; Sowers, A. L.; Cook, J. A.; Baum, B. J.; Krishna, M. C.; Mitchell, J. B. Differential radiation protection of salivary glands versus tumor by tempol with accompanying tissue assessment of tempol by magnetic resonance imaging. *Clin. Cancer Res.* **2007**, *13*, 4928–4933.

(17) Zhang, L.; Zhu, H.; Oprea, T. I.; Golbraikh, A.; Tropsha, A. QSAR modeling of the blood-brain barrier permeability for diverse organic compounds. *Pharm. Res.* **2008**, *25*, 1902–1914.

(18) Shen, D. D.; Artru, A. A.; Adkison, K. K. Principles and applicability of CSF sampling for the assessment of CNS drug delivery and pharmacodynamics. *Adv. Drug Delivery Rev.* **2004**, *56*, 1825–1857.

membranes, etc.) often serve as a major approach for indirect evaluation of drug delivery in the brain tissue. The development of new methodologies for *in vivo* imaging of BBB permeability, which are noninvasive, environmentally friendly, with minimal animal loss and minimal risk for volunteers, is a major goal of the modern pharmaceutical industry.

Currently, the radiopharmaceuticals combined with autoradiography or positron-emission tomography (PET) are the only option for noninvasive real-time imaging of BBB permeability.[23−25] Despite that this approach is highly sensitive and valuable, it suffers from several restrictions to be widely applicable in preclinical and clinical testing of new therapeutics. The radiolabeling possesses a risk for human safety and requires special experimental equipment and facilities, which increases markedly the cost of this analysis. The radiotracers are usually used for labeling of diagnostic markers, but not for labeling of therapeutics and noninvasive imaging of their permeability and localization in different organs.

In the present study, we would like to introduce a novel nonradioactive and environmentally friendly alternative for noninvasive real-time imaging of BBB permeability for conventional drugs, using stable nitroxyl radicals as spin-labels and MRI. To clarify the advisability of this approach, we have to prove that (i) the nitroxyl-labeled drug is stable in physiological fluids and there is no dissociation of nitroxyl-drug bond in the blood; and (ii) the nitroxyl-labeling does not affect significantly the drug pharmacodynamics, its toxicity and permeability for BBB.

We considered the anticancer drug lomustine [1-(2-chloroethyl)-3-cyclohexyl-1-nitrosourea, CCNU] as an appropriate model for spin-labeling and nitroxyl radical TEMPO as an appropriate spin-label for this particular case. Lomustine has a significant impact in the improvement of the health-related quality of life of patients, treated for brain tumors, as well as of any other patients with cancer.[26] Both substances (TEMPO-radical and lomustine) are permeable for BBB,[16,27] and the TEMPO radical has a 6-membered ringed structure as the cyclohexyl part of lomustine molecule.

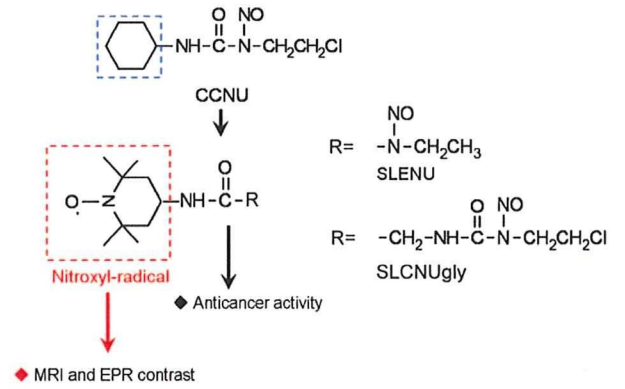

Figure 1. (A) Lomustine (CCNU) and its nitroxyl-labeled analogues (SLENU and SLCNUgly).

The lomustine molecule could be formally separated into two parts (Figure 1). The nitrosourea ensures the anticancer effect and could not be modified. Thus, the cyclohexyl part of lomustine was exchanged with TEMPO radical. We supposed that this substitution keeps a low risk for influence of drug pharmacodynamics in the organism, its toxicity and anticancer effect.

Two TEMPO-labeled analogues (SLENU and SLCNUgly) of lomustine (originally synthesized) (Figure 1) and one commercial nitroxyl (TEMPOL) were used in EPR and MRI experiments. All substances were characterized with different hydrophobicity [classified as slightly hydrophobic (TEMPOL), hydrophobic (SLENU), and strongly hydrophobic (SLCNUgly)], cell permeabilization ability and blood clearance. Thus, it was possible to investigate the relationship between the structure of nitroxyl-labeled drug, its half-life in the circulation, its permeability for BBB and MRI signal dynamic in the brain. This information was important for estimation of the merits and demerits of the described approach and finding pathways for overcoming the restrictions.

Experimental Methods

Chemicals. TEMPOL (4-hydroxy-2,2,6,6-tetramethyl-1-piperidin-1-oxyl) was purchased from Sigma-Aldrich.

Nitroxyl-labeled nitrosoureas SLENU {1-ethyl-3-[4-(2,2,6,6-tetramethylpiperidine-1-oxyl)]-1-nitrosourea} and SLCNUgly {1-chloroethyl-3-[4-glycine-(2,2,6,6-tetrameth-

(19) Pan, D.; Iyer, M.; Liu, J.; Li, Y.; Hopfinger, A. J. Constructing optimum blood brain barrier QSAR models using a combination of 4D-molecular similarity measures and cluster analysis. *J. Chem. Inf. Comput. Sci.* **2004**, *44*, 2083–2098.
(20) Dash, A. K.; Elmquist, W. F. Separation methods that are capable of revealing blood-brain barrier permeability. *J. Chromatogr., B: Anal. Technol. Biomed. Life Sci.* **2003**, *797*, 241–254.
(21) Gumbleton, M.; Audus, K. L. Progress and limitations in the use of in vitro cell cultures to serve as a permeability screen for the blood-brain barrier. *J. Pharm. Sci.* **2001**, *90*, 1681–1698.
(22) Killian, D. M.; Gharat, L.; Chikhale, P. J. Modulating blood-brain barrier interactions of amino acid-based anticancer agents. *Drug Delivery* **2000**, *7*, 21–25.
(23) Josserand, V.; Pélerin, H.; de Bruin, B.; Jego, B.; Kuhnast, B.; Hinnen, F.; Ducongé, F.; Boisgard, R.; Beuvon, F.; Chassoux, F.; Daumas-Duport, C.; Ezan, E.; Dollé, F.; Mabondzo, A.; Tavitian, B. Evaluation of drug penetration into the brain: a double study by in vivo imaging with positron emission tomography and using an in vitro model of the human blood-brain barrier. *J. Pharmacol. Exp. Ther.* **2006**, *316*, 79–86.
(24) Abbott, N. J.; Chugani, D. C.; Zaharchuk, G.; Rosen, B. R.; Lo, E. H. Delivery of imaging agents into brain. *Adv. Drug Delivery Rev.* **1999**, *37*, 253–277.
(25) Weissleder, R.; Mahmood, U. Molecular imaging. *Radiology* **2001**, *219*, 316–333.
(26) Taphoorn, M. J. B.; Van den Bent, M. J.; Mauer, M. E. L.; Coens, C.; Delattre, J.-Y.; Brandes, A. A.; Smitt, P. A. E.; Besrnsen, H. J. J. A.; Frenay, M.; Tijssen, C. C.; Lacombe, D.; Allgeier, A.; Bottomley, A. Health-related quality of life in patients treated for anaplastic oligodendroma with adjuvant chemotherapy: Results of a European Organisation for Research and Treatment of Cancer Randomized Clinical Trial. *J. Clin. Oncol.* **2007**, *25*, 5723–5730.
(27) Bodor, N.; Buchwald, P. Recent advances in the brain targeting of neuropharmaceuticals by chemical delivery systems. *Adv. Drug Delivery Rev.* **1999**, *36*, 229–254.

ylpiperidine-1-oxyl)]-1-nitrosourea} were synthesized and purified according to Gadjeva et al.[28,29] (with slight modifications).

Deionized water (deionization by the Milli-Q system) was used for all experiments. Other chemicals used were of analytical or HPLC grade.

***In Vitro* EPR measurements.** SLENU, SLCNUgly, and TEMPOL were first dissolved in DMSO to prepare 200 mM stock solutions. These 200 mM solutions were diluted with PBS, containing 1% bovine serum albumin to prepare 2 mM standard solutions. Each solution was put into a glass capillary, and their X-band EPR spectra were measured on X-band EPR instrument (JEOL, Akishima, Japan) with a TE-mode cavity. The capillary tube was positioned in the center of the TE-mode cavity using a special sample holder. The measurements were made under the following conditions: microwave frequency = 9.4 GHz, magnetic field strength = 336 mT, microwave power = 2.0 mW, field modulation frequency = 100 kHz, field modulation amplitude = 0.063 mT, time constant = 0.01 s, sweep width = 10 mT, scan time (sweep time) = 1 min.

In parallel, 2 μL of 200 mM stock solutions of SLENU, SLCNUgly, or TEMPOL (in DMSO) were added to 198 μL freshly isolated blood (with heparin) and the EPR measurements were provided at the parameters mentioned above within 30 min scan time.

The rotational correlation time (τ_c) of nitroxyl derivatives in PBS and blood was calculated by the following equation (Figure 2):[30]

$$\tau_c = A\{R(-1) + R(+1) - 2\} \cdot \Delta H(0) \qquad (1)$$

$R(-1) = [I(0)/I(-1)]^{1/2}$, where $I(0)$ and $I(-1)$ are the amplitudes of line 2 and line 3 in the EPR spectrum, respectively; $R(+1) = [I(0)/I(+1)]^{1/2}$, where $I(0)$ and $I(+1)$ are the amplitudes of line 2 and line 1 in the EPR spectrum, respectively; $\Delta H(0)$ is a line 2 width; $A = 6.6 \times 10^{-10}$ s is a constant, calculated for TEMPO radical.

All calculations were made from the EPR spectra of the nitroxyl derivatives (2 mM) in PBS or freashly isolated blood from mouse (after 5 min incubation). In the text, the data are presented as mean values from three independent experiments (SD did not exceed 5%). The obtained values are approximated, since we used an A-value for TEMPO in all calculations.

The total nitroxyl concentration in the brain tissue was analyzed according to Hyodo et al.[10] In brief, the brain was isolated 10 min after the iv injection of nitroxyl derivative in the mouse (0.4 mmol/kg bw). The isolated brain was

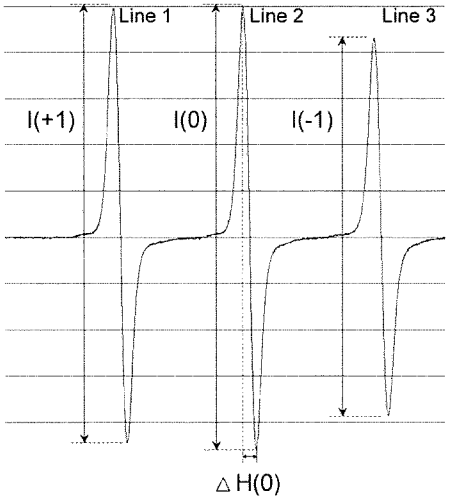

Figure 2. X-band EPR spectrum of TEMPO radical in PBS (pH 7.4) and characteristics used in the calculation of the rotational correlation time (τ_c).

rinsed several times by cold PBS, and the tissue (in equal weight for each animal) was homogenized in cold PBS. Ferricyanide (200 μL of 10 mM solution) was added to each homogenate (800 μL) to convert the reduced nitroxyl derivatives to their oxidized forms. EPR signal intensity was measured in tissue homogenates under the following conditions: modulation frequency, 100 kHz; microwave power, 1 mW. Finally, the concentration of nitroxyl derivative in the brain tissue was calculated based on a dilution factor of 5.

***In Vivo* EPR measurements.** The pharmacokinetic profiles of nitroxyl derivatives in mouse blood were measured using the method reported by Matsumoto et al.[31] C57Bl/6 mice (6 to 8 weeks of age at the time of experiments; mean weight ~25 g) were used. All experiments were conducted in accordance with the guidelines of the Physiological Society of Japan and were approved by the Animal Care and Use Committee of the National Institute of Radiological Sciences, Chiba, Japan.

The experimental design is shown in Scheme 2.

The mouse (~25 g) was anesthetized with 1.5% isoflurane using a face mask. The body temperature was kept within 36 ± 1 °C. The tail and jugular veins were cannulated by polyethylene tubing (PE10, Intramedic, Becton Dickinson Co.). The PE10 tubing from the jugular vein was placed in the TE-mode cavity of EPR instrument (JEOL, Akishima, Japan). The end of the tubing was connected to the syringe. All tubing and syringes were heparinized. The nitroxyl derivative was injected intravenously through the tail vein (0.4 mmol/kg bw; the drugs were dissolved in DMSO), and immediately after the injection the blood (~100 μL) was drained from the blood stream through the jugular vein to

(28) Gadjeva, V. Structure-based design of nitrosoureas containing tyrosine derivatives as potential antimelanoma agents. *Eur. J. Med. Chem.* **2002**, *37*, 295–300.

(29) Zheleva, A.; Gadjeva, V. Spin labelled nitrosoureas and triazenes and their non-labelled clinically used analogues--a comparative study on their physicochemical properties and antimelanomic effects. *Int. J. Pharmacol.* **2001**, *212*, 257–266.

(30) Hayashi, H.; Iwasaki, T.; Onodera, Y.; Nagase, T.; Itabashi, O. *Tohoku Kogyo Gijitsu Shikenjo Houkoku* **1992**, *29*, 33.

(31) Matsumoto, K.; Krishna, M. C.; Mitchell, J. B. Novel pharmacokinetic measurement using electron paramagnetic resonance spectroscopy and simulation of in vivo decay of various nitroxyl spin probes in mouse blood. *J. Pharmacol. Exp. Ther.* **2004**, *310*, 1076–1083.

Scheme 2. Scheme of Imaging of EPR Signal Dynamic of Nitroxyl Radical in the Blood Stream of Mouse under Anesthesia

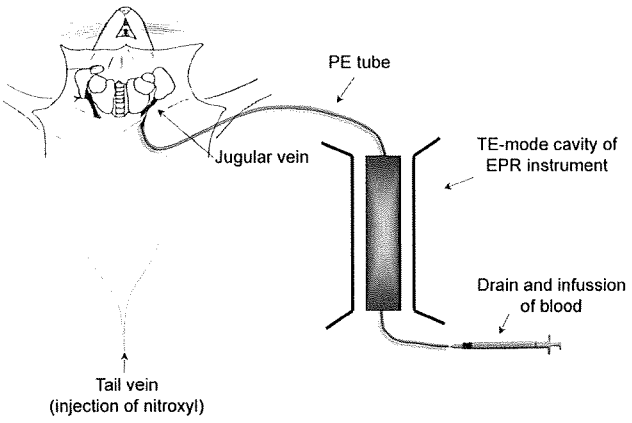

reach the TE-mode cavity of the EPR instrument. The EPR measurement was started. Immediately after finishing the measurement, the blood was infused back to the blood stream of the mouse. This cycle was repeated every 4−5 min within 30 min, to register the EPR signal dynamic of nitroxyl radical after its intravenous injection in the anesthetized animal. The EPR measurements were carried out in the same manner as described above.

***In Vivo* MRI Measurements.** MRI measurements were performed on a 7.0 T horizontal magnet (Kobelco and Jastec, Japan) interfaced to a Bruker Avance console (Bruker BioSpin, Germany) and controlled with ParaVision 4.0.1 (Bruker BioSpin, Germany).

The mouse (C57Bl/6, ~25 g) was anesthetized by isoflurane (1.2%) and placed in a head holder (Rapid Biomedical, Germany), stomach-side down and fixed head. A respiration sensor (SA Instruments, NY) was placed on the back of the mouse. A nonmagnetic temperature probe (FOT-M and FTI-10, FISO Technology, Germany) was used to monitor the rectal temperature of the mouse. The tail vein was cannulated by polyethylene tubing (PE10, Becton-Dickinson, NJ, USA) for injection of drug. The mouse was then placed in the ^{1}H-volume radiofrequency (RF) resonator (Brucker BioSpin) with surface RF receiver (Rapid Biomedical, Germany), which was previously warmed up using a body temperature controller (Rapid Biomedical). The resonator units, including the mouse, were placed in the magnet bore. The mouse body temperature was kept at 37 ± 1 °C during the MR measurements. Before the measurements after drug injection, five control images of the mouse brain were taken with the following parameters: T_1-weighted incoherent gradient-echo sequence (fast low-angle shot; FLASH), repetition time (TR) = 75 ms; echo time (TE) = 3.5 ms; flip angle (FA) = 45 degrees; field of view (FOV) = 3.2 × 3.2 cm; number of averages = 4; scan time = 19.6 s; matrix = 64 × 64; slice thickness = 1.0 mm; number of slices = 4. We selected coronal slice orientations with a 500 μm × 500 μm × 1000 μm nominal voxel resolution. One minute and 40 s after starting the scan, 100 μL of SLENU, SLCNUgly or TEMPOL (final dose, 0.4 mmol/kg bw; the drugs were dissolved in DMSO) was injected via the tail vein. T_1-weighted images were acquired continuously within ~20 min.

Mice, injected with DMSO only (in the same volume, 100 μL) served as controls.

The MRI data were analyzed using the ImageJ (National Institutes of Health, MD, USA) software.

All experiments were conducted in accordance with the guidelines of the Physiological Society of Japan and were approved by the Animal Care and Use Committee of the National Institute of Radiological Sciences, Chiba, Japan.

Results and Discussion

The substitution of the cyclohexyl part of the lomustine molecule with nitroxyl radical, as well as the substitution at the fourth position of the piperidine ring, did not affect significantly the toxicity and anticancer activity of nitrosourea. Using wild-type C57Bl/6 mice, we established the following LD50 values for nitroxyl derivatives: ~210 mg/kg bw for TEMPOL, ~100 mg/kg bw for SLENU, and ~125 mg/kg bw for SLCNUgly, versus ~56 mg/kg bw for lomustine (CCNU). The nitroxyl radical in SLENU and SLCNUgly decreased the toxicity of nitrosourea.

Using C57Bl/6 mice with experimental lymphoma L1210, we established the following optimal doses for anticancer activity of SLENU, SLCNUgly, and CCNU: ~45 mg/kg bw for SLENU and SLCNUgly, versus ~20 mg/kg for CCNU.

These preliminary data allowed the selection of the optimal dose for *in vivo* EPR and MR imaging of nitroxyl derivatives in C57Bl/6 mice. The doses, combining a comparatively low toxicity and comparatively high EPR and MRI contrast characteristics, were in the interval 0.2−0.4 mmol/kg bw, below the toxic limit or slightly close to the LD50 values of the described nitroxyl derivatives.

The first step of our study was to ensure that the TEMPO−nitrosourea bond is stable and there is no dissociation between both compounds in the blood. Thus, the detection of MRI signal enhancement of nitroxyl radical *in vivo* will indicate the localization of nitrosourea in the brain tissue.

In PBS, the normalized EPR spectra of TEMPOL, SLENU, and SLCNUgly were distinguished by the amplitude of the third line in the triplet [$I(-1)$] (Figure 3A). The lower amplitudes of line 3 in the EPR spectrum of SLENU and SLCNUgly could be explained by the limited motion of the nitrosourea-conjugated nitroxyl radical in comparison with free TEMPO radical (in the TEMPOL molecule). The larger the substitute at the fourth position of the piperidine ring, the slower the motion of the nitroxyl radical, which results in lower EPR signal enhancement. In PBS, the rotational correlations times (τ_c) of nitroxyl derivatives were 10.56 × 10^{-12} s, 29.45 × 10^{-12} s, and 31.38 × 10^{-12} s for TEMPOL, SLENU, and SLCNUgly, respectively.

In blood, the normalized EPR spectra had the same profiles as in PBS. There were no changes in the shape of the EPR spectra of SLENU and SLCNUgly during long-term incuba-

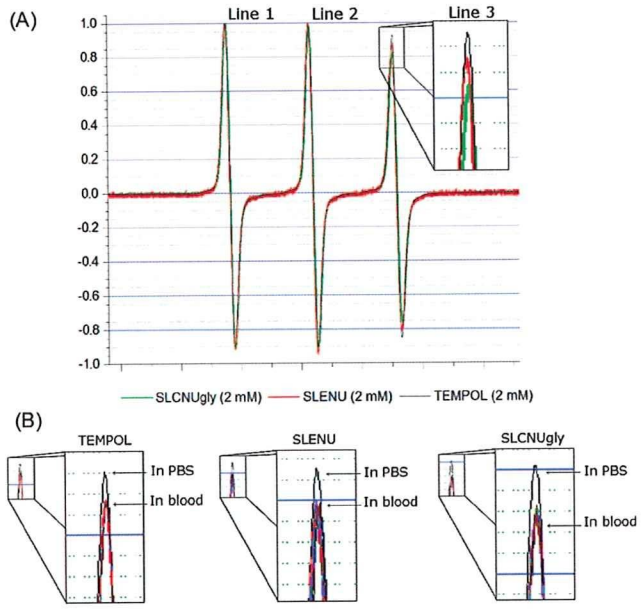

Figure 3. (A) Normalized EPR spectra of SLENU, SLCNUgly, and TEMPOL in PBS. In blood, the EPR spectra of all substances have same profiles. (B) Amplitudes of line 3 during long-term incubation of SLENU, SLCNUgly, and TEMPOL in freshly isolated blood samples *in vitro* (1−30 min). The amplitude of line 3 in PBS is shown for comparison.

tion in blood (Figure 3B), which indicated that there was no dissociation of the TEMPO−nitrosourea covalent bond. Only the amplitude of line 3 decreased in blood in comparison with PBS (Figure 3B). The rotational correlations times (τ_c) of nitroxyl derivatives in blood were 20.33×10^{-12} s, 32.87×10^{-12} s, and 46.20×10^{-12} s for TEMPOL, SLENU, and SLCNUgly, respectively. The data suggest that the motion of nitroxyl radical in blood decreased for each derivative, regardless of its hydrophobicity, presumably as a result of interaction between the drug and blood cells and/or lipoproteins.

In the second step, we investigated the blood clearance of nitroxyl derivatives *in vivo* in mice, using EPR spectroscopy (Scheme 2). This information allowed a prediction of the time necessary for transportation of nitroxyl derivative in the brain tissue (if it crosses BBB), which was important for design of the MRI measurements.

The kinetic curves of EPR signal dynamics of nitroxyl derivatives in the blood stream of living mice are shown in Figure 4. They were characterized with two phases: (i) an increase of the EPR signal within 1−1.5 min after the drug injection; and (ii) a decrease of the EPR signal within 1−5 min after the drug injection. The first phase is mainly a result of initial enhancement of the drug concentration in the blood stream. The second phase is probably a result of the following processes: (i) a reduction of nitroxyl radical in the blood plasma; and/or (ii) transportation of the drug from the blood stream to the blood cells and/or tissues and further reduction of nitroxyl radical from the cell/tissue reducing equivalents.

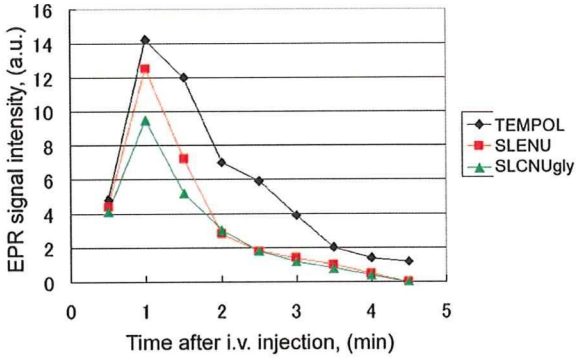

Figure 4. Dynamics of the EPR signal in the blood stream of mice under anesthesia after intravenous (iv) injection of nitroxyl derivative (0.4 mmol/kg bw). Mean values from three independent experiments are presented in the figure (SD values did not exceed 30%).

The time-decay of the EPR signal *in vivo* correlated with the hydrophobicity of nitroxyl derivative and its cell permeability. The rate of time-decay was slower for the low hydrophobic TEMPOL and faster for the hydrophobic SLENU and strongly hydrophobic SLCNUgly.

In vivo, the EPR signal of all nitroxyl derivatives disappeared rapidly in the blood (within 4−5 min after their injection). However, *in vitro* (in isolated blood samples), their EPR signal was comparatively stable within 1−30 min incubation (only ~5% decrease was detected within this time interval). Since all investigated nitroxyls were cell permeable, we may speculate that within 4−5 min the nitroxyl derivatives were delivered in the tissues.

In the third step of our study, the nitroxyl derivatives were injected intravenously in healthy mice via the tail vein and ^{1}H-MR imaging of the brain was performed on a 7.0 T horizontal MRI (Figure 5). The injected dose was 0.4 mmol/kg bw.

At the selected scanning parameters, the nitroxyl-radical manifested a good T_1 relaxivity and was detected in the brain (Figure 5). Other authors[8,9] have also demonstrated a good T_1 relaxivity of TEMPOL at similar concentrations on experimental phantoms and animals (mice) using 4.7 T MRI and high image resolution (128 × 128 or 256 × 256). Although nitroxyls have a lower relaxivity than conventional T_1 contrast agents such as gadolinium complexes, the volume distribution of nitroxyls is sufficiently greater because of better cell permeability,[35] and with improved sensitivity of

(32) Matsumoto, K.; Yakumaru, H.; Narazaki, M.; Nakagawa, H.; Anzai, K.; Ikehira, H.; Ikota, N. Modification of nitroxyl contrast agents with multiple spins and their proton T_1 relaxivity. *Magn. Reson. Imaging* **2008**, *26*, 117–121.

(33) Metz, J. M.; Smith, D.; Mick, R.; Lustig, R.; Mitchell, J.; Cherakuri, M.; Glatstein, E.; Hahn, S. M. A phase I study of topical Tempol for the prevention of alopecia induced by whole brain radiotherapy. *Clin. Cancer Res.* **2004**, *10*, 6411–6417.

(34) Ravizza, R.; Cereda, E.; Monti, E.; Gariboldi, M. B. The piperidine nitroxide Tempol potentiates the cytotoxic effects of Temozolomide in human glioblastoma cells. *Int. J. Oncol.* **2004**, *25*, 1817–1822.

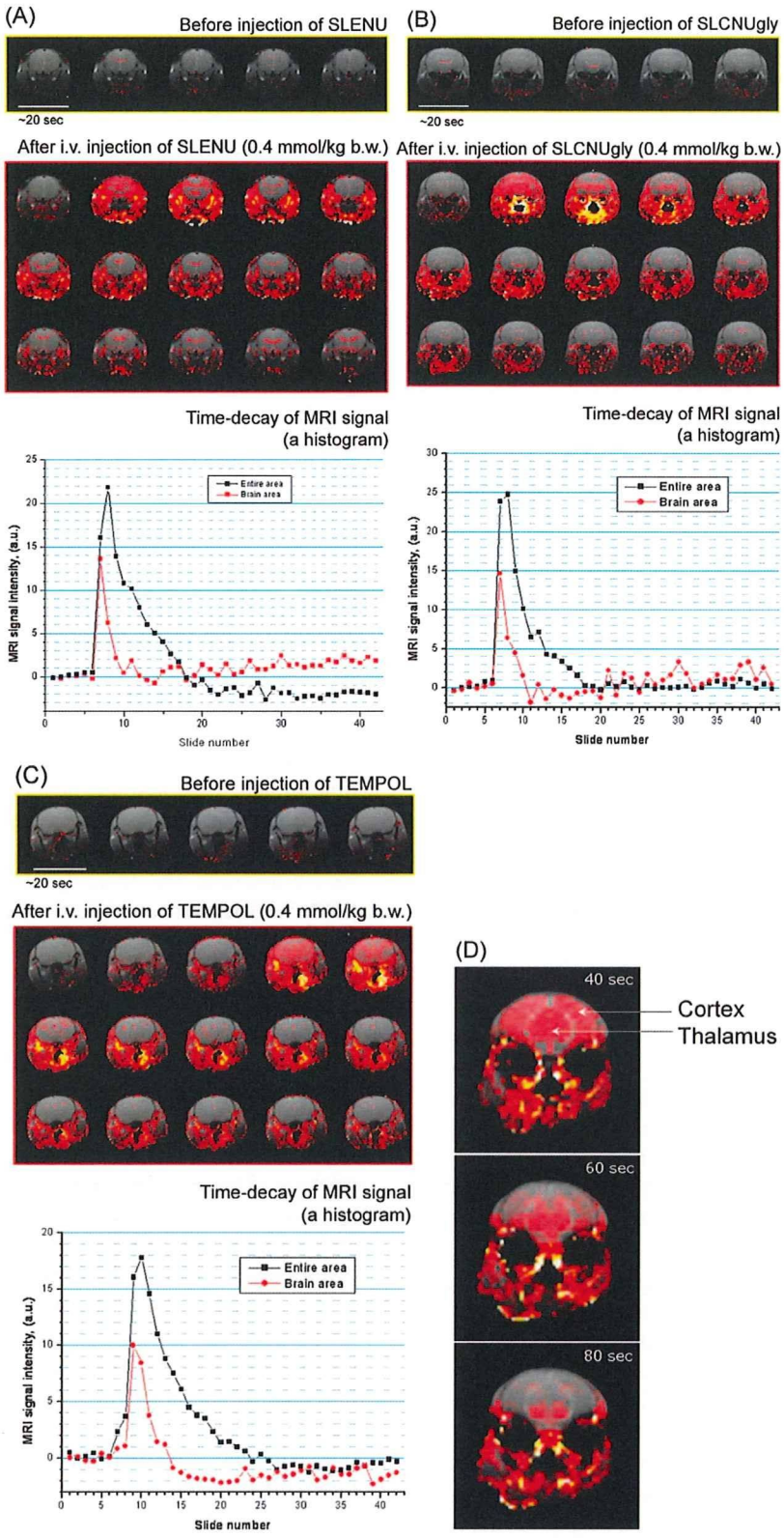

Figure 5. MRI signal dynamics of SLENU (A), SLCNUgly (B), and TEMPOL (C) in the brain and surrounding tissues after iv injection in mice (0.4 mmol/kg bw). Each image was obtained within a 20 s interval using a gradient-echo T_1-weighted MRI. The red color in the images is the extraction of the signal between every single slide and the averaged baseline signal (first 5 slides: before injection). The red and black colors in the chart represent MRI signal dynamics in the brain or entire area, respectively. A representative image from three independent experiments is shown in the figure. (D) MRI signal dynamics of SLENU in the brain compartments (cortex and thalamus) after its iv injection in mice (0.8 mmol/kg bw).

MRI and shift to higher magnetic fields, it is possible to detect nitroxyl radical in the tissues at low (nontoxic or low toxic) concentrations. In our study, using 7 T MRI and resolution 64 × 64, the MRI contrast of TEMPOL was high enough to detect the signal in the brain at concentrations 0.4 mmol/kg bw.

It is well-known that the nitrosoureas are highly permeable for cell membranes and BBB and are concentrated in the brain tissue. Therefore, it could be expected that the real concentration of SLENU and SLCNUgly in the brain tissue would be same as or even higher than the concentration of TEMPOL, and this should have a positive effect on MRI contrast of both nitroxyl-labeled drugs. We established that ~30% of the injected dose of SLENU and SLCNUgly was localized in the brain. The experiments were performed on tissue homogenates prepared from perfused brain, isolated 10 min after the iv injection of the drug.

The MRI-signal dynamics of SLENU and SLCNUgly (Figure 5A,B) in the brain and surrounding tissues followed almost the same kinetics and distribution as nonconjugated TEMPO radical (Figure 5C). The maximum change in the signal intensity (~25−30% in comparison with the preinjection image) in the brain tissue was detected 20, 20 or 80 s after the injection of SLENU, SLCNUgly, or TEMPOL, respectively. In the brain tissue, the MRI signal intensity decreased during the subsequent 2 min, while in the surrounding tissues, the MRI signal intensity decreased during the subsequent 4−5 min. Recently, Hyodo et al. have reported that the MRI signal of a BBB permeable nitroxyl, methoxycarbonyl-2,2,5,5-tetramethylpyrrolidine-1-oxyl, also disappeared quickly after its transportation from the blood vessels to the brain tissue, despite the slower reduction rate of pyrrolidine radical.[11]

SLENU and SLCNUgly were rapidly and randomly distributed into the brain tissue. For example, the nitroxyl derivatives were localized predominantly in the cortex and thalamus (Figure 5D). The MRI signal decay in the cortex was faster than the MRI signal decay in the thalamus. It may be speculated that the cortex has a higher reduction potential than the thalamus. Similar results were reported by Hyodo et al.[11]

Obviously, the exchange of the cyclohexyl part of lomustine with TEMPO radical did not suppress the permeability of the drug for the BBB. All investigated nitroxyl derivatives (TEMPOL, SLENU, SLCNUgly) manifested a similar permeability. This assumption was confirmed by using EPR spectroscopy for the assessment of the total concentration of nitroxyl derivative (converted to its oxidized form) in the brain tissue, isolated 10 min after the drug injection into mice. It was observed that the normalized EPR signal intensity of tissue homogenates, isolated from SLENU- and SLCNUgly-treated mice (2.3 ± 0.6 and 2.5 ± 0.4 a.u. per g of tissue, respectively), was slightly higher than the EPR signal intensity of homogenates, isolated from TEMPOL-treated mice (2.0 ± 0.5 a.u. per g of tissue). The data from diffusion-weighted MRI also confirmed that SLENU and SLCNUgly crossed the BBB. After free-water signal suppression by the diffusion-weighted MRI technique with motion probing gradients, the MRI signal remained in the brain tissue (data are not shown).

The MRI signal enhancement of nitroxyl radical disappeared quickly (within 2−3 min) after the transportation of SLENU and SLCNUgly from the brain vessels in the brain tissue. Presumably, this is due to the high permeability of nitroxyl-labeled nitrosoureas for cell membranes, which is accompanied with rapid reduction of nitroxyl radical to the respective hydroxylamine in the brain cells and loss of MRI signal enhancement. In the surrounding tissues, the MRI signal was more stable, with a bit longer half-life.

There was a good correlation between the rate of blood clearance of nitroxyl derivatives and their MRI signal dynamic in the brain and surrounding tissues. The faster the blood clearance of the drug (SLCNUgly = SLENU > TEMPOL), the faster the appearance of the MRI signal of the nitroxyl derivative in the brain and surrounding tissues (SLCNUgly = SLENU > TEMPOL) (Figures 4, 5).

The fast detection of MRI signal enhancement could be considered as an advantage, because of shortening of the time of analytical and diagnostic process.

The present data are just a first trial for using nitroxyl radicals for spin-labeling of conventional drugs and noninvasive dynamic MR imaging of their permeability for the BBB. We tried to show the advisability of this concept. Novel synthetic strategies are necessary to increase the contrast of nitroxyl label and to improve its stability in the brain tissue without affecting the drug permeability for BBB. This will allow a higher spatial resolution of signal-to-noise ratio and will facilitate the real-time MRI data reconstruction and quantitative analysis.

The enhancement of the MRI contrast of nitroxyl label is important for the wide application of the described methodology. This is a limiting factor, currently requiring the application of nitroxyl-labeled drug in a comparatively high concentration (0.2−0.4 mmol/kg bw), which sometimes could be near or over the toxic limit.

There are two promising strategies to increase the MRI contrast of nitroxyl label in the brain and other tissues: (i) the exchange of six-membered ringed nitroxyl TEMPO with five-membered ringed nitroxyl (2,2,5,5-tetramethyl-pyrrolidinyl-1-oxyl, PROXYL), which is characterized by higher relaxivity and ~10 times higher resistance to bioreduction than TEMPO radical;[2] and (ii) to develop new nitroxyl probes by modification of nitroxyl contrast agents with multiple spins (2 or more nitroxyl radicals bound covalently).

Matsumoto and colleagues have reported that a probe, consisting of three covalently bound PROXYL radicals, is characterized with 4-fold higher T_1 relaxivity than a single PROXYL radical. However, it is still unclear whether these multinitroxyl probes are permeable for BBB, cells and other tissues, to be applicable for labeling of conventional drugs

(35) Hahn, S. M.; Wilson, L.; Krishna, C. M.; Liebmann, J.; DeGraff, W.; Gamson, J.; Amuni, A.; Venzon, S.; Mitchell, J. Identification of nitroxide radioprotectors. *Radiat. Res.* **1992**, *123*, 87–93.

and noninvasive imaging of their localization in the organism. The low-molecular-weight cell- and BBB-permeable methoxycarbonyl-PROXYL seems promising for drug labeling and MR imaging in the brain. Recently, Hyodo and colleagues have used this nitroxyl derivative for evaluation of brain redox status by MRI. The MRI signal of methoxycarbonyl-PROXYL in the brain is comparatively high and stable within 4 min after the drug injection in mice. Our preliminary data also demonstrated that PROXYL is characterized with higher MRI contrast and slower MRI signal decay in the tissues (Figure 1S, Supporting Information). Currently, we are under way to clarify the applicability of PROXYL in the described methodology.

It is necessary also to note that nitroxyl radicals are low toxic and comparatively harmless for living organisms. One of the most famous commercially available nitroxyls, TEMPOL (hydroxyl-TEMPO), is in phase I of clinical trials, as a preventer of alopecia in radiation-treated cancer patients.[32] The combined application of nitroxyls and conventional chemotherapeutics increases the anticancer effect and suppresses the multidrug resistance.[33] Therefore, the nitroxyl-labeling could be considered as environmentally friendly and with minimal risk for humans. There is one more advantage in nitroxyl-labeling and imaging. The dynamic of MRI signal enhancement gives additional information for oxidation/reduction status of the brain tissue. This information could be useful for planning of conventional chemo- and radiotherapy of cancer and other diseases in the brain or other organs.

Acknowledgment. The technical support of Dr. Antoaneta Zheleva (Trakia University, Stara Zagora, Bulgaria) and Ms. Sayaka Shibata (Molecular Imaging Center, NIRS-Chiba, Japan) is gratefully acknowledged.

Supporting Information Available: Figure depicting the MRI signal dynamics of carbamoyl-PROXYL in the brain after iv injection in mice. This material is available free of charge via the Internet at http://pubs.acs.org.

MP800175K

Neuroscience Research 65 (2009) 64–70

Contents lists available at ScienceDirect

Neuroscience Research

journal homepage: www.elsevier.com/locate/neures

Effect of cyclooxygenase-2 on the regulation of cerebral blood flow during neuronal activation in the rat

Tetsuya Matsuura [a,b,*], Hiroyuki Takuwa [b], Rumiana Bakalova [b], Takayuki Obata [b], Iwao Kanno [b]

[a] Academic Group of Mathematical and Natural Science, Iwate University, 4-3-5 Ueda, Morioka 020-8551, Japan
[b] Department of Biophysics, Molecular Imaging Center, National Institute of Radiological Sciences, 4-9-1 Anagawa, Chiba 263-8555, Japan

ARTICLE INFO

Article history:
Received 23 February 2009
Received in revised form 9 May 2009
Accepted 15 May 2009
Available online 23 May 2009

Keywords:
Cerebral blood flow
Cyclooxygenase-2
Functional activation
Laser-Doppler flowmetry
Somatosensory stimulation
Rat

ABSTRACT

The present study was designed to clarify the precision of the main approach for investigating the regulation of local cerebral blood flow (CBF) response to neuronal activation in the brain (neurovascular coupling). In this study, we examined the effects of NS-398, a highly selective cyclooxygenase-2 inhibitor, on the physiological variables, baseline CBF, and local CBF response during rat somatosensory neuronal activation by laser-Doppler flowmetry. Blood pressure and heart rate were significantly decreased 3 h after i.v. infusion of NS-398. Baseline CBF and local CBF during somatosensory activation gradually decreased with an increase in time of NS-398 infusion up to 3 h, although neuronal activity in the somatosensory area was almost constant during the infusion. The results suggest that cyclooxygenase-2 participates in the regulation of local CBF during neuronal activation in rats. The present study also revealed the potential side-effects of dimethylsulfoxide, a solvent of NS-398, on neurovascular coupling.

1. Introduction

The tight spatial and temporal coupling of neuronal activity with local cerebral blood flow (CBF), which is known as neurovascular coupling, is a hallmark of brain function (Magistretti et al., 1999; Iadecola, 2004). Functional hyperemia occurs within seconds of neuronal activation and is spatially coupled to brain areas with increased energy demand (Chaigneau et al., 2003; Lauritzen, 2005). Any damage to the neurovascular coupling mechanism is accompanied by disturbance of brain cell homeostasis and provokes brain pathology and cell death. Clarifying the key molecular targets underlying the regulation of neurovascular coupling and controlling them could present a consequential way of increasing the life of brain cells, overcoming neurodegenerative diseases, and delaying the process of senescence.

The commonly accepted hypothesis is that local vasodilation in response to neuronal activity depends on the activation of astrocytes by locally released neurotransmitters. Many biochemical substances mimic the role of triggers and key mediators of neurovascular coupling. However, the data are usually controversial, the major reason being that investigations of this life science phenomenon are based on indirect approaches. At least three biochemical pathways of astrocyte-mediated vasodilation act like triggers (Bakalova et al., 2002; Ances, 2004; Girouard and Iadecola, 2006; Phillis et al., 2006; Takano et al., 2006; Wang et al., 2006): (i) arachidonic acid cascade; (ii) nitric oxide cascade; (iii) adenosine-mediated pathway. In addition, other substances such as Ca^{2+}, H^{+}, carbon dioxide, and carbon oxide are also related to the vasodilation pathway.

In the present study, we focused on the products of the arachidonic acid cascade as one of the critical triggers or secondary regulators of neurovascular coupling in the brain. Our reason for this was based mainly on the unique lipid composition of rat brain tissue. Approximately 90% of rat brain cell membranes of synapses and astrocytes consist only of polyunsaturated lipids, composed of arachidonic acid, docosahexaenoic acid (DHA), and eicosapentaenoic acid (EPA) residues (Kagan et al., 1992; Chalon et al., 2001; Yehuda et al., 2002; Solfrizzi et al., 2005). There are no other animal tissues with such lipid composition. Arachidonic acid is a precursor of prostaglandins, DHA of docosanoids, and EPA of eicosanoids. It is well known that all neurodegenerative diseases are accompanied by a significant decrease of these polyunsaturated fatty acids (PUFAs) in the brain, as well as by an imbalance in their metabolites (Kagan et al., 1992; Yehuda et al., 2002; Solfrizzi et al., 2005). Therefore, the metabolites of PUFAs could be selected as priority molecular targets in investigations of the regulatory mechanisms of neurovascular coupling. However, it is necessary to note that the reason for the unique lipid composition of brain

* Corresponding author at: Department of Welfare Engineering, Faculty of Engineering, Iwate University, 4-3-5 Ueda, Morioka 020-8551, Japan.
Tel.: +81 19 621 6376; fax: +81 19 621 6376.
E-mail address: matsuura@iwate-u.ac.jp (T. Matsuura).

0168-0102/$ – see front matter © 2009 Elsevier Ireland Ltd and the Japan Neuroscience Society. All rights reserved.
doi:10.1016/j.neures.2009.05.006

membranes could be simpler than the reasons mentioned above. Neurotransmission requires a permanent dynamic of brain biomembranes, which are obligatory for continuous transport of neurotransmitters and neuromediators. Thus, brain membranes have to be flexible and permeable, which is ensured through their polyunsaturated lipid structure.

The aim of the present study is to affirm the role of the arachidonic acid cascade in the local CBF response to neuronal activity (neurovascular coupling) and to clarify the precise mechanism of this regulation. In this study, we examined the effects of NS-398, a highly selective cyclooxygenase-2 inhibitor (an inhibitor of prostaglandin synthesis), on CBF regulation during somatosensory neuronal activation in rats by laser-Doppler flowmetry. The present study also revealed the potential side-effects of dimethylsulfoxide (DMSO), a solvent of NS-398, on neurovascular coupling.

2. Materials and methods

2.1. Animal preparation

All experiments were conducted in accordance with the guidelines of the Physiological Society of Japan and were approved by the Animal Care and Use Committee of the National Institute of Radiological Sciences, Chiba, Japan.

Twenty-two Sprague–Dawley male rats (385.4 ± 3.2 g) were used to investigate the effect of NS-398 (selective inhibitor of cyclooxygenase-2 isoenzyme, COX-2) and DMSO (a solvent of NS-398) on the CBF response. The NS-398-treated group consisted of thirteen rats, and the DMSO-treated group, used as a control, consisted of nine rats. The rats were anesthetized with isoflurane (4.0% for induction and 1.5% during surgery) in 15% O_2 and 85% air using a face mask. Subcutaneous 2% lidocaine was used before incision to prevent vasospasm during catheter insertion. Polyethylene catheters were used to cannulate the tail artery and the left femoral vein for blood pressure monitoring, blood sampling for gas analysis, and i.v. administration of anesthetic and NS-398 (or DMSO). After tracheotomy, α-chloralose (50 mg/kg, i.v.) was injected, and isoflurane administration was discontinued. Anesthesia was maintained with α-chloralose (45 mg/(kg h), i.v.) and muscle relaxation with pancronium bromide (0.7 mg/(kg h), i.v.). Body temperature was monitored with a rectal probe and maintained at about 37.0 °C using a heating pad (ATC-210, Unique Medical, Japan). During the experiment, the rats were ventilated by respirator (SN-480-n, Shinano, Japan) with a mixture of air and oxygen to achieve physiological arterial blood levels of PaO_2 and $PaCO_2$ ($PaCO_2$ of 33–40 mmHg and PaO_2 of 110–130 mmHg) by regulating the stroke volume of ventilation and the fractional concentration of oxygen in the inspired gas, respectively.

Each rat was fixed in a stereotactic frame, and the parietal bone was thinned to translucency over the left somatosensory cortex using a dental drill (an area of 3 mm × 3 mm, centered at 2.5 mm caudal and 2.5 mm lateral to the bregma). To ensure a stable physiological condition of the animal, the measurements were performed for 3 h after preparation of the parietal bone. The depth of anesthesia was controlled by continuous monitoring of mean arterial blood pressure (MABP) and heart rate during the stabilization period (Fig. 1). The rate of α-chloralose infusion was constant during the measurements after a 3-h adaptation period.

2.2. LDF measurement and hind paw stimulation

The increase in local CBF response during hind paw stimulation (evoked CBF) was measured by LDF (FLO-C1, OMEGA FLO, Japan). The tip diameter of the LDF probe was 0.55 mm (Probe NS, OMEGA FLO). LDF was used to measure red blood cell behavior in capillaries based on the Doppler-effect with laser light (wavelength of 780 nm). The frequency-shift of scattered radiation was caused by the movement of red blood cells in the blood vessels. The sampling volume of LDF measurement was about 1 mm^3 (Solfrizzi et al., 2005). A time constant of 0.1 s was used to detect the LDF signal.

The LDF probe was positioned over the thinned skull (over the somatosensory area of the hind paw) perpendicular to the brain surface. It was attached to the thinned parietal bone and then finely positioned using a micromanipulator to obtain the

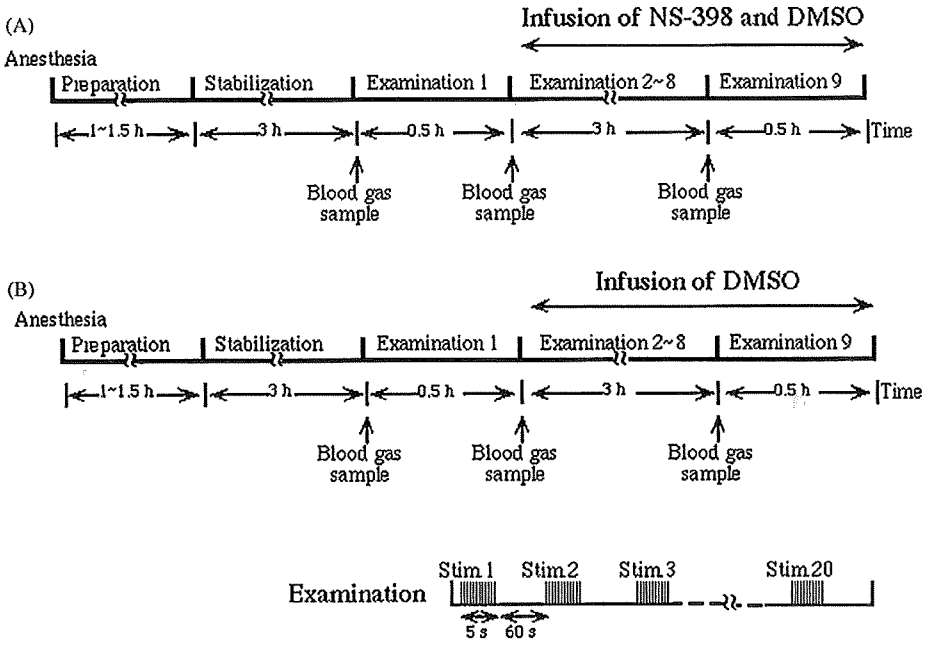

Fig. 1. Experimental protocol of i.v. administration of NS-398 dissolved in DMSO (A) and that of only DMSO (B). The experiment was started about 3 h after the preparation of the animal. The evoked CBF response was examined before and after drug administration. At each examination, 20 successive pulses of 5 Hz (5-s duration, 1.5 mA) were applied at 60 s intervals.

maximum signal change during stimulation (15–20% at frequency of 5 Hz, currency of 1.5 mA, duration of 5 s), avoiding areas with large blood vessels.

Electrical hind paw stimulation was performed with 2 needle electrodes inserted subdermally into the right hind paw (at the plantar and ankle regions, respectively) contralaterally to the LDF probe. In all rats, a current stimulus of 1.5 mA (0.1 ms pulse) was applied at a frequency of 5 Hz for a 5-s duration. At each examination, 20 successive pulses were applied at 60 s intervals (Fig. 1).

The choice of stimulation parameters was based on previously published data (Ngai et al., 1995; Detre et al., 1998; Matsuura et al., 1999, 2000; Matsuura and Kanno, 2001). In hemodynamic studies on rats, it has been reported that the increase in stimulus frequency up to approximately 5 Hz caused a linear increase in the evoked CBF, although its further enhancement (above 5 Hz) led to a decrease in evoked CBF response. It is well known that in the evoked CBF response curves, during long periods of stimulation, there is an initial peak followed by a plateau (Ngai et al., 1995; Detre et al., 1998; Matsuura and Kanno, 2001). It is assumed that the initial peak reflects an early transient reaction to neuronal activity.

2.3. Preparation and application of NS-398

NS-398 (50 mg; Cyaman Chemicals, USA) was first dissolved in 2 ml DMSO. Immediately before infusion, 0.1 ml DMSO, which included NS-398 (2.5 mg), was added to 12 ml saline solution (approximately 0.6 mM) according to the manufacturer's recommendations. The concentrations of NS-398 and DMSO were proper quantities in respect to the physiological condition (tracer concentration) (Takano et al., 2006).

The experimental protocol is shown in Fig. 1. In the first experimental group, NS-398 was applied intravenously–continuous infusion with 0.4 mg/(kg h) (Fig. 1A). In some experiments, continuous NS-398 infusion with 0.2 or 0.8 mg/(kg h) was also applied to examine the dose dependence of the effects on systemic and CBF response. As a control group, 0.1 ml DMSO was added to 12 ml saline solution, and it was applied using the same protocol as that of the NS-398 infusion (Fig. 1B). The rate of both infusions was 0.7 ml/h.

2.4. Examination of neuronal activity during application of NS-398

To confirm the presence of neuronal activity during somatosensory stimulation under NS-398 infusion with 0.4 mg/(kg h), the evoked field potentials (FP) were recorded in 6 rats. The spontaneous neuronal activity (spontaneous FP) was also determined during DMSO or NS-398 infusion with 0.4 mg/(kg h) ($n = 5$). The tip of the electrode was set at a depth of about 0.5 mm from the surface of the cortex. An Ag–AgCl indifferent electrode was placed between the skull bone and the scalp. Twenty successive signals of the evoked FP recordings were accumulated using a MacLab data acquisition software (Scope) (AD Instruments, Australia). In the evoked FP analysis, we calculated the sum of the amplitude of field potential as an index of the integrated neuronal activity (Matsuura and Kanno, 2001). The spontaneous FP was recorded by the MacLab data acquisition software (Chart), and the frequency of field potential, which had greater amplitude than that of the noise level, was calculated. Data were digitized at 100 Hz.

2.5. Data analysis

Arterial blood pressure was monitored and MABP was calculated during the experiments. Arterial blood samples were serially collected at three time points, before examination 1, before infusion of NS-398 or DMSO, and 3 h after infusion, and samples were analyzed for blood gas values.

The LDF signal and arterial blood pressure were recorded continuously on MacLab data acquisition software, and the outputs from 20 successive measurements were accumulated. Data were digitized at 100 Hz and saved on a disk for off-line analysis. The rise-time and termination-time of evoked CBF were defined as the times at the intersection of the extrapolated lines, which were drawn on the response curve from 90% to 10% of the peak from the baseline (Bakalova et al., 2002). The rise-time is a hemodynamic latency, being the time at which the evoked CBF curve leaves the baseline level after the onset of stimulation. The peak-time is the time at which the response curve of evoked CBF reaches the maximum amplitude. The termination-time is the time at which the evoked CBF curve returns to the baseline level after maximum response. The LDF-signal was normalized towards the baseline level as percent changes from the baseline, and was defined as "normalized evoked CBF" in the present paper. The normalized evoked CBF curves before and after NS-398 infusion were superimposed by the baseline level using software (KalidaGraph 3.5, Synergy Software, UAE). The response magnitude of normalized evoked CBF was calculated as an integral of the response curve

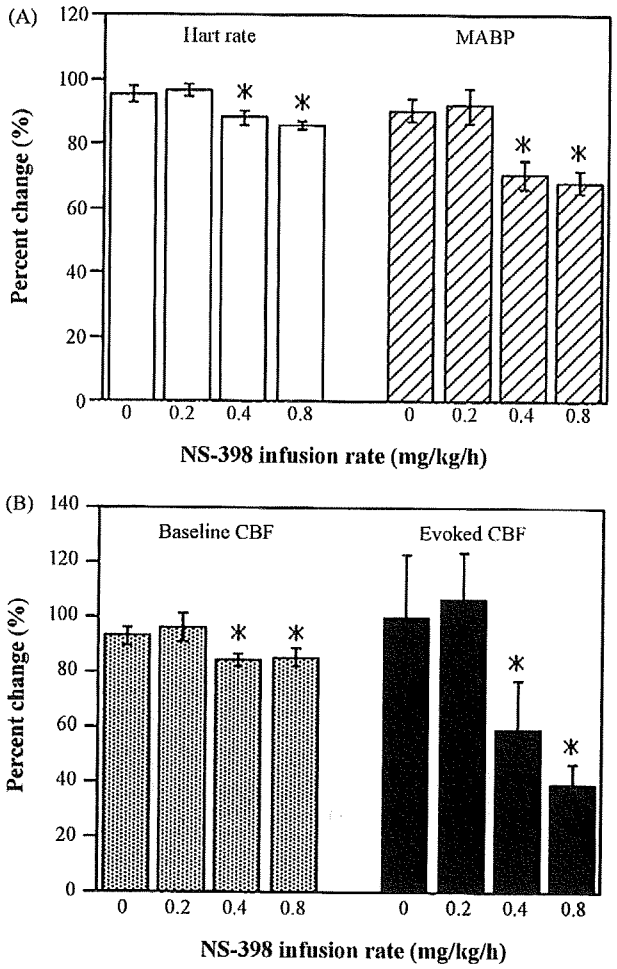

Fig. 2. Effects of NS-398 concentration on the physiological parameters (A), and baseline CBF and response magnitudes of normalized evoked CBF (B). Each column indicates percent changes in values compared between before and 3 h after NS-398 infusion of various concentrations, and zero column shows a value of percent change during DMSO infusion (control). Asterisks indicate that there are statistically significant differences in values between before and 3 h after infusion ($p < 0.05$). Error bars are SEM ($n \geq 5$).

Table 1
Physiological parameters.

	Heart rate (beats/min)	MABP (mmHg)	$PaCO_2$ (mmHg)	PaO_2 (mmHg)
NS-398 infusion ($n = 13$)				
Before	389.9 ± 7.1	113.5 ± 3.8	34.8 ± 0.8	114.5 ± 5.5
3 h after infusion	343.3 ± 8.8**	80.2 ± 5.8**	35.9 ± 0.9	116.5 ± 6.7
DMSO infusion ($n = 9$)				
Before	366.5 ± 7.2	107.2 ± 4.8	35.5 ± 1.1	100.73 ± 3.1
3 h after infusion	348.9 ± 9.6	97.1 ± 5.1	36.3 ± 1.5	99.9 ± 3.6

Mean ± SEM. **$p < 0.01$

from the rise-time to the termination-time (Matsuura et al., 1999; Bakalova et al., 2002).

Values were statistically analyzed by Student's *t*-test and are presented as mean ± SEM.

3. Results

3.1. Effects of NS-398 concentration on physiological variables and evoked CBF

The effect of NS-398 on evoked CBF response was the greatest at 3 h infusion (see below). Therefore, we showed the percent changes in physiological parameters, baseline CBF and normalized evoked CBF, which were compared between before and 3 h after NS-398 infusion.

DMSO infusion and NS-398 infusion with 0.2 mg/(kg h) did not significantly affect any of the physiological parameters (Fig. 2A). On the other hand, there were significant decreases in MABP and heart rate between before and 3 h after infusion ($p < 0.05$) when NS-398 was infused with 0.4 or 0.8 mg/(kg h). The $PaCO_2$ and PaO_2 values were not changed by NS-398 infusion (data not shown).

When NS-398 was infused with 0.2 mg/(kg h), changes in baseline CBF and response magnitude of normalized evoked CBF were almost the same as those of DMSO infusion. When NS-398 was infused with 0.4 or 0.8 mg/(kg h), the baseline CBF was suppressed by NS-398 infusion ($p < 0.05$), and response magnitudes of normalized evoked CBF were also suppressed with an increase in NS-398 concentration ($p < 0.05$) (Fig. 2B). In the experiments below, the infusion rate of NS-398 was fixed at 0.4 mg/(kg h) as a tracer concentration.

3.2. Effect of NS-398 and its solvent on physiological variables

As shown in Table 1, MABP and heart rate were significantly decreased 3 h after i.v. infusion of NS-398, but the $PaCO_2$ and PaO_2 values were not affected by NS-398. COX inhibitors are well-known vasoconstrictors and these effects were expected. DMSO did not significantly affect any of the physiological parameters (Table 1).

The kinetic curves of MABP and heart rate dynamics demonstrated that both parameters gradually decreased with increasing time of NS-398 infusion within 0.5–3.5 h (Fig. 3). On the other hand, MABP and the heart rate of the control group were constant within 0.5–2 h of DMSO infusion (Fig. 3). A slight gradual decrease in MABP and the heart rate was observed after 2 h of DMSO infusion, although a statistically significant difference was not detected (Table 1).

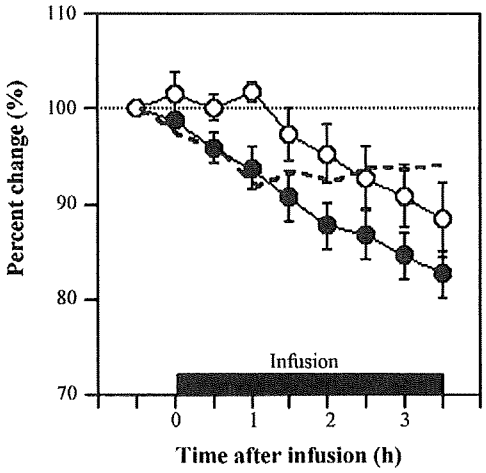

Fig. 4. Changes in baseline CBF after continuous infusion of NS-398 (closed circles; $n = 13$) or its solvent, DMSO (open circles; $n = 9$). Error bars indicate SEM. Dotted line indicates the subtraction of the mean values of baseline CBF changes in the DMSO-treated group from the mean values in the NS-398-treated group.

3.3. Effect of NS-398 and its solvent on baseline CBF

Baseline CBF gradually decreased within 0.5–3.5 h of NS-398 infusion, with a maximum decrease of approximately 18.38 ± 2.47% at 3.5 h (Fig. 4). On the other hand, baseline CBF was constant within 0.5–1.5 h of DMSO infusion and decreased gradually between 1.5 and 3.5 h. In this case, the maximum decrease of baseline CBF would be 11.66 ± 3.90% at 3.5 h of DMSO infusion. These results indicate that the real effect of NS-398 on baseline CBF could be distinguished within the 0.5–1.5-hour interval. When the effect of DMSO (mean values of open circles in Fig. 4) is actually subtracted

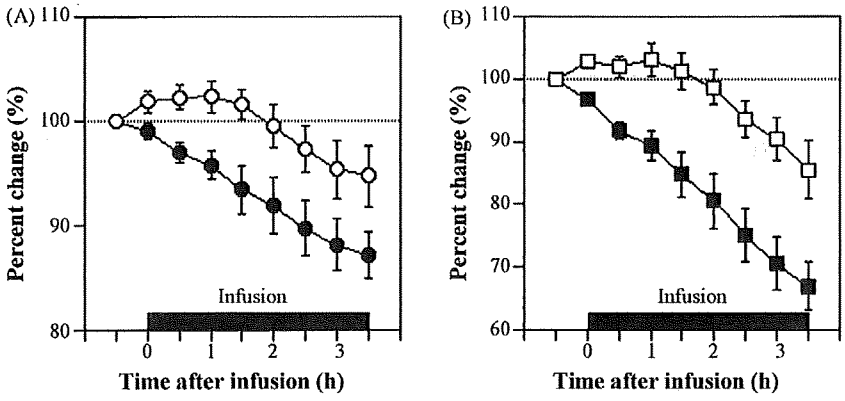

Fig. 3. Changes in heart rate (A) and MABP (B) after continuous infusion of NS-398 (closed circles and squares; $n = 13$) or its solvent DMSO (open circles and squares; $n = 9$). Error bars indicate SEM.

from the effect of NS-398 (mean values of closed circles), it seems that the baseline CBF decreases within 1 h of infusion of COX-2 inhibitor and reaches a plateau within 1–3.5 h (dotted line).

3.4. Effect of NS-398 and its solvent on local CBF response to neuronal activity

To evaluate the neuronal activity of the somatosensory area during the experiments, spontaneous neuronal activity (spontaneous FP) and evoked neuronal activity (evoked FP) were determined. There was no significant difference in frequency of the spontaneous FP between before and after DMSO or NS-398 infusion (Fig. 5). The somatosensory neuronal activity to hind paw stimulation (evoked FP) was also almost constant during the entire time-interval (before and 0.5–3.5 h after NS-398 infusion) (Fig. 6). The results suggest that the level of anesthesia was almost constant during the period of measurements.

The normalized evoked CBF decreased with an increase in time of NS-398 infusion up to 3 h (Fig. 7A). The response curves had the same profile both before and after the drug administration. NS-398 did not affect the peak-time and termination-time of the evoked CBF, although the rise-time increased significantly at 3 h of NS-398 infusion (Table 2). DMSO infusion did not affect any time-parameters of the evoked CBF (Table 2).

The detailed statistical analysis of the response magnitude of normalized evoked CBF with the time of NS-398 or DMSO infusion is shown in Fig. 7B. In the case of NS-398, the normalized evoked CBF decreased gradually within 1.5 h of infusion, reaching a plateau after 1.5 h. When the response magnitudes of normalized evoked CBF after NS-398 infusion were compared with those

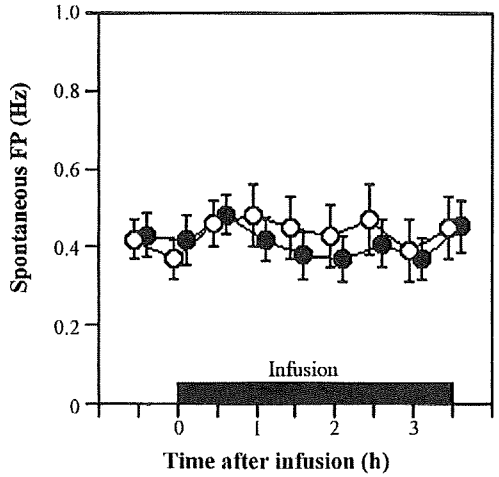

Fig. 5. Spontaneous neuronal activity during DMSO or NS-398 infusion. Open and closed circles were frequencies of spontaneous FP during DMSO and NS-398 infusion, respectively. Note that there was no obvious difference in spontaneous FP during DMSO or NS-398 infusion. Error bars indicate SEM ($n = 5$).

before infusion, a significant decrease in the normalized evoked CBF was observed at 3 h after NS-398 infusion (Fig. 7B). In the case of DMSO, the normalized evoked CBF was almost constant within 3 h of infusion and increased slightly after 3.5 h (Fig. 7B). The comparative analysis of response magnitudes of normalized evoked CBF at each time-point demonstrated that the effect of NS-398 on normalized evoked CBF was not significant within 2 h

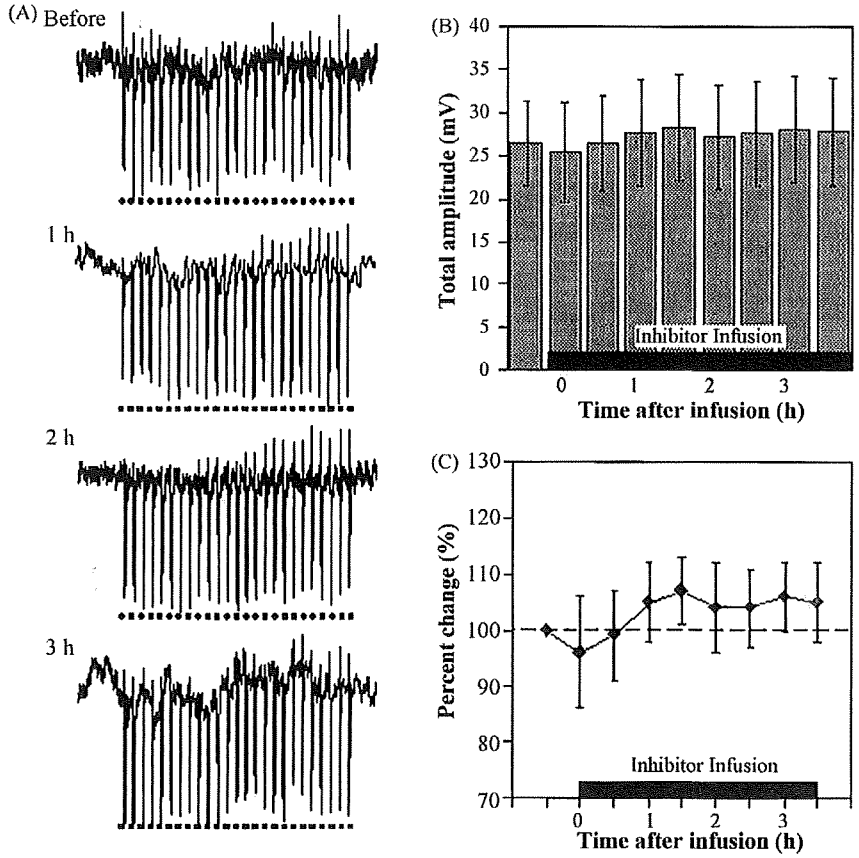

Fig. 6. Evoked neuronal activity during NS-398 infusion. (A) Example of evoked FP. (B) Total amplitude of evoked FP. (C) Percent changes in the total amplitude of evoked FP. Note that the somatosensory neuronal activity to hind paw stimulation was almost constant. Error bars indicate SEM ($n = 6$).

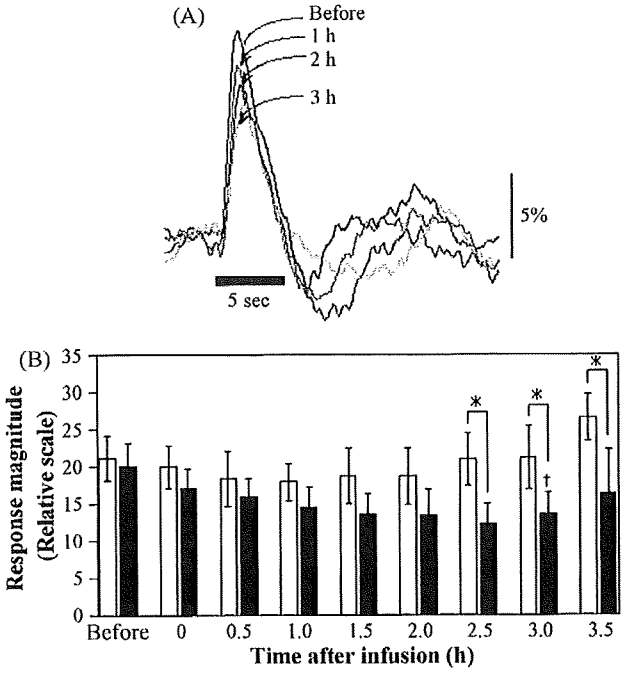

Fig. 7. Changes in normalized evoked CBF after continuous infusion of NS-398. (A) Normalized evoked CBF in response to somatosensory stimulation before and after continuous infusion of NS-398. The response curves are normalized to the baseline level of CBF and averaged by the number of animals used ($n = 13$). The curves were superimposed by the baseline level using software. Horizontal and vertical bars indicate stimulation period (5 s) and percent increase compared to that of the baseline level (5%), respectively. (B) Response magnitude of normalized evoked CBF at each time-point. Open and closed columns indicate the normalized magnitude of DMSO-treated animals ($n = 9$) and NS-398-treated animals ($n = 13$), respectively. When the normalized evoked CBF after NS-398 infusion was compared with that before infusion, a significant decrease in magnitude of normalized evoked CBF was observed ($^{\dagger}p < 0.05$). Note that a significant decrease in evoked CBF was detected from 2.5 h of COX-2 inhibitor infusion. Error bars indicate SEM. $^{*}p < 0.05$.

Table 2
Time-parameters of evoked CBF response curves.

	Rise time (s)	Peak time (s)	Termination time (s)
NS-398 infusion ($n = 13$)			
Before	0.45 ± 0.04	2.07 ± 0.18	5.69 ± 0.47
3 h after infusion	0.66 ± 0.08*	2.09 ± 0.15	5.76 ± 0.54
DMSO infusion ($n = 9$)			
Before	0.43 ± 0.04	1.70 ± 0.13	6.22 ± 0.44
3 h after infusion	0.49 ± 0.05	1.84 ± 0.06	5.22 ± 0.37

Mean ± SEM. $^{*}p < 0.05$

of infusion. A statistically significant decrease in response magnitudes of normalized evoked CBF was detected after COX-inhibitor infusion within 2.5–3.5 h (Fig. 7B).

4. Discussion

The present experiment was designed to clarify the effect of COX-2 on the regulation of cerebral blood flow, and it revealed that COX-2 participates in the regulation of baseline CBF and normalized evoked CBF in the rat. The present study also revealed the potential side-effects of DMSO, a solvent of COX-2 inhibitor, on neurovascular coupling. To the best of our knowledge, this is the first report to detect the efficacy of COX-2 inhibitor on CBF regulation by i.v. infusion. The approach of a neurovascular coupling study is usually used for drugs that could inhibit or activate specifically the major biochemical pathways. Some of these drugs have low water-solubility and have to be dissolved in non-physiological solution, such as dimethylsulfohide (DMSO), dimethylformamide, NaOH, or ethanol. However, even at tracer concentrations, these solvents may influence neurovascular coupling by themselves and could mimic the real effect of the inhibitor or activator on the biochemical target, which is crucial for interpretation of the experimental data.

DMSO is one of the most commonly used organic solvents for intravenous infusion of non-adhesive liquids. DMSO is also considered to function as a central nervous system (CNS) protector against ischemia and trauma. Recently, Dudeck et al. (2006) reported that DMSO does not manifest angiotoxic effects. However, it has been reported that intravenous infusion of DMSO in doses which provide CNS protection (~2 g/kg) changes some systemic parameters in experimental animals (Hameroff et al., 1981; Del Bigio et al., 1982). Immediately after infusion, DMSO causes an enhancement of heart rate, pulmonary capillary wedge pressure and pulmonary arterial (systolic, mean, and diastolic) pressures, and a decrease of systemic diastolic pressure and systemic vascular resistance (Hameroff et al., 1981). Most DMSO induced changes are reversible and return towards pre-infusion values 10 min after the end of infusion (Hameroff et al., 1981). Similar data have been published also by Del Bigio et al. (1982).

In our study, as a control examination, DMSO was administered at the same volume as that of NS-398 infusion. DMSO did not provoke any side-effects in the physiological variables within 2 h of continuous infusion (Table 1 and Fig. 3). Slight decreases in MABP and heart rate were observed after 2.5 h of DMSO infusion, although there was no significant difference in these physiological variables between before and after DMSO infusion (Table 1). In our previous study, we confirmed that the depth of anesthesia was almost constant and did not affect the physiological variables during 3 h of measurement (Matsuura and Kanno, 2001). These observations suggest the potential side-effects of DMSO on the physiological variables and neurovascular coupling. Therefore, it could be concluded that, during 2 h of NS-398 infusion, the decrease in MABP and heart rate were provoked predominantly by COX-2 inhibitor (Fig. 3). Artifacts in the investigation of baseline CBF and normalized evoked CBF as a result of systemic changes could be minimal within 2 h of infusion of COX-2 inhibitor. Within this time-interval, there is a minimal possibility of accumulation of large amounts of NS-398 and DMSO metabolites, which could non-specifically influence the physiological variables, homeostasis and microcirculation. On the other hand, by the time of 2.5 h of NS-398 infusion, it may be difficult to distinguish the real effect of COX-inhibitor from the side-effects of solvents and drug metabolites on physiological variables. Thus, neurovascular coupling experiments using more than 2 h of NS-398 infusion could lead to misinterpretations. In any event, it is clear that COX-2 inhibitor experiments need comparison with control measurements using a single infusion of a solvent.

Comparing physiological data, as described above, it is necessary to note that the real effect of NS-398 on evoked CBF could be distinguished from the side-effects of solvent and/or metabolites within 2 h of infusion. In this time-interval, we observed slight, non-significant suppression of the normalized evoked CBF by NS-398. Takano et al. (2006) investigated the effect of NS-398 (0.6 mM) on astrocyte-mediated vasodilation and found that COX-2 inhibitor had no effect. In contrast, Niwa et al. (2000) observed that the increase in CBF to vibrissal somatosensory stimulation is attenuated by topical superfusion with NS-398 (0.1 mM). Unfortunately, neither group described the details of drug preparation and application, preventing a thorough analysis of this discrepancy. Probably, both data are correct and the discrepancies are a result of different experimental protocols, including different conditions of preparation and administration of COX-2 inhibitor.